

Wave-equation migration velocity analysis using plane-wave common image gathers

Bowen Guo* and Gerard T. Schuster*

** Department of Earth Science and Engineering,*

King Abdullah University of Science and Technology,

Thuwal, Saudi Arabia, 23955-6900.

Email: bowen.guo@kaust.edu.sa; gerard.schuster@kaust.edu.sa.

(December 6, 2016)

Running head: **Plane-wave WEMVA**

ABSTRACT

Wave-equation migration velocity analysis (WEMVA) based on subsurface-offset, angle domain or time-lag common image gathers (CIGs) requires significant computational and memory resources because it computes migration images with extra dimensions in the extended image domain. To mitigate this problem, a WEMVA method using plane-wave CIGs is presented. Plane-wave CIGs reduce the computational cost and memory storage because they are directly calculated from prestack plane-wave migration, and the number of plane waves is much less than the number of shots. In the case of an inaccurate migration velocity, the moveout of plane-wave CIGs is automatically picked by a semblance analysis method, which is then linked to the migration velocity update by a connective function. Numerical tests on two synthetic datasets and a field dataset validate the efficiency and effectiveness of this method.

INTRODUCTION

An accurate estimate of the background velocity model is important to obtain focused images with migration. Wave-equation migration velocity analysis (WEMVA) (Biondi et al., 1999; Mulder and Ten Kroode, 2002; Sava and Biondi, 2004; Shen and Symes, 2008) inverts for the migration velocity using a non-linear iterative scheme that maximizes the similarities of a collective of images at the same location. This image group is referred to as common image gathers (CIGs), with at least three types: angle-domain (Xu et al., 2001; Sava and Fomel, 2003; Biondi and Symes, 2004), subsurface-offset (Rickett and Sava, 2002) and time-lag CIGs (Sava and Fomel, 2006).

Subsurface-offset and time-lag CIGs require an extended imaging condition in the space-lag and time-lag domain for each shot. Besides the physical dimensions in x-y-z, an extended image for a single shot has extra dimensions for space or time lags, which requires a significant increase in memory storage space. Angle-domain CIGs are computed by a slant stack of the subsurface-offset CIGs (Sava and Fomel, 2003), or by calculating wavefield propagation directions during migration (Xu et al., 2011; Dickens and Winbow, 2011; Zhang, 2014). The final CIGs result from stacking all the shot gathers together. Computing these CIGs for WEMVA has a high computational cost and memory storage requirement for large 3D datasets.

To mitigate this problem, plane-wave migration (Whitmore, 1995; Duquet et al., 2001; Zhang et al., 2005; Liu et al., 2006) can be applied to form plane-wave CIGs. This method combines multiple shot gathers into a composite plane-wave gather and migrates the plane-wave gathers with different ray parameters p to obtain plane-wave CIGs. The benefit is that there is no need for the extra dimensions in the extended image domain. Moreover,

the number of plane waves is much less than the number of shots in the survey. Because of these two reasons, plane-wave CIGs save computational cost and memory space compared to CIGs in other domains.

Plane-wave technology has been used in the exploration geophysics community to save computational cost in full waveform inversion (Vigh and Starr, 2008) and least-squares migration (Dai and Schuster, 2013; Wang et al., 2014). Jiao et al. (2002) applied residual migration velocity analysis in the plane-wave domain, where the migration velocities were scanned and picked to flatten plane-wave CIGs by a moveout correction based on an analytical moveout formula. However, this formula is only valid for a 1D velocity model or a 2D model with small dip angles.

To overcome this limitation, we present a WEMVA method using plane-wave CIGs, denoted as PWEMVA. PWEMVA inverts for the migration velocity by minimizing the objective function which is the squared summation of the local shifts between a plane-wave migration image and a reference image. This objective function is based on the principle that an accurate migration velocity leads to horizontally aligned CIGs for different p values. The local shift at a given image point is computed by choosing a parabola which best fits the moveout of the plane-wave CIG. Similar approaches have been used by Zhang and Biondi (2013) and Zhang et al. (2015), except for that they extracted the moveout of the shot and angle-domain CIGs. A connective function (Luo and Schuster, 1991) is used to link the local shifts with the velocity update so that the gradient of the objective function is derived.

After the introduction, the theory section summarizes the theory of plane-wave migration, introduces the objective function ϵ of the PWEMVA method and derives the gradient

of ϵ . The formula for updating the velocity model is given and a workflow is presented for implementing the PWEMVA method. This is followed by the numerical results section which presents the results of applying PWEMVA to synthetic data and a marine data set recorded in the Gulf of Mexico. The last two sections include the discussions and conclusions.

THEORY

Plane-wave migration

For a 2D medium, let $S_k(\omega, \mathbf{x})$ represent the source-side wavefield of a single shot located at $(x_k, z = 0)$ at the surface. The plane-wave source-side wavefield $\bar{S}(\omega, \mathbf{x})$ is the summation of all the delayed shot wavefields from single shots:

$$\bar{S}(\omega, \mathbf{x}) = \sum_{k=1}^{n_s} e^{i\omega p(x_k - x_0)} S_k(\omega, \mathbf{x}), \quad (1)$$

where n_s represents the shot number, i is the imaginary unit, ω denotes the angular frequency and $(x_0, 0)$ is the location at the surface where the plane-wave is initiated at $t = 0$. Here, $p = \sin \theta / v$ is the ray parameter of the plane wave, where θ is referred to as the shooting angle and v is the velocity at the surface.

Similarly, the plane-wave receiver-side wavefield $\bar{R}(\omega, \mathbf{x})$ is the summation of all the delayed backward-extrapolated receiver-side wavefields $R_k(\omega, \mathbf{x})$ excited by the source wavefield $S_k(\omega, \mathbf{x})$:

$$\bar{R}(\omega, \mathbf{x}) = \sum_{k=1}^{n_s} e^{i\omega p(x_k - x_0)} R_k(\omega, \mathbf{x}). \quad (2)$$

This plane-wave receiver wavefield at the receiver position \mathbf{x}_g is referred to as a plane-wave

gather.

The prestack plane-wave migration image is obtained by multiplying the plane-wave source-side wavefield with the complex conjugate of the receiver-side wavefield in the frequency domain and summing over all frequencies:

$$m(\mathbf{x}) = \Re \left\{ \sum_{\omega} \bar{S}(\omega, \mathbf{x}) \bar{R}(\omega, \mathbf{x})^* \right\}, \quad (3)$$

where $\Re\{\}$ represents the real part.

Objective function and gradient

The objective function ϵ for PWEMVA is defined as the squared summation of the vertical local shift $\Delta w_j(\mathbf{x}_0)$ between two patches $B(\mathbf{x}_0)$ centered at \mathbf{x}_0 of a plane-wave migration image m_j and the reference image m_0 :

$$\epsilon = \frac{1}{2} \sum_{j=1}^{n_p} \sum_{\mathbf{x}_0 \in B} \Delta w_j(\mathbf{x}_0)^2, \quad (4)$$

where j denotes the plane-wave index, n_p represents the number of plane waves and B stands for the set of all patches in the migration image. The local vertical shift $\Delta w_j(\mathbf{x}_0)$ aligns $m_0(x, z + \Delta w_j(\mathbf{x}_0))$ with $m_j(x, z)$ for $\mathbf{x} \in B(\mathbf{x}_0)$, where $B(\mathbf{x}_0)$ is of the width and height of a wavelength.

The gradient of the objective function with respect to the slowness $c(\mathbf{x}')$ (reciprocal of the migration velocity) is

$$\frac{\partial \epsilon}{\partial c(\mathbf{x}')} = \sum_{j=1}^{n_p} \sum_{\mathbf{x}_0 \in B} \frac{\partial \Delta w_j(\mathbf{x}_0)}{\partial c(\mathbf{x}')} \Delta w_j(\mathbf{x}_0). \quad (5)$$

In order to calculate the Fréchet derivative of the local shift of the window centered at \mathbf{x}_0 with respect to the slowness perturbation at \mathbf{x}' , a connective function is defined as the local cross-correlation between $m_0(B(\mathbf{x}_0))$ and $m_j(B(\mathbf{x}_0))$:

$$f_j(c(\mathbf{x}'), w_j(\mathbf{x}_0)) = \sum_{\mathbf{x} \in B(\mathbf{x}_0)} m_0(x, z + w_j(\mathbf{x}_0)) m_j(x, z), \quad (6)$$

where $\mathbf{x} = (x, z)$ and $w_j(\mathbf{x}_0)$ is a random local shift. The correct image shift $\Delta w_j(\mathbf{x}_0)$ aligns $m_0(x, z + \Delta w_j(\mathbf{x}_0))$ with $m_j(x, z)$ within $B(\mathbf{x}_0)$, so that the connective function in equation 6 is maximized. This means that the derivative of f_j with respect to $w_j(\mathbf{x}_0)$ should be zero at $\Delta w_j(\mathbf{x}_0)$:

$$\begin{aligned} \bar{f}_j(c(\mathbf{x}'), \Delta w_j(\mathbf{x}_0)) &= \sum_{\mathbf{x} \in B(\mathbf{x}_0)} \left. \frac{\partial f_j(c(\mathbf{x}'), w_j(\mathbf{x}_0))}{\partial w_j(\mathbf{x}_0)} \right|_{w_j(\mathbf{x}_0) = \Delta w_j(\mathbf{x}_0)} \\ &= \sum_{\mathbf{x} \in B(\mathbf{x}_0)} m_j(x, z) \dot{m}_0(x, z + \Delta w_j(\mathbf{x}_0)) \\ &= 0, \end{aligned}$$

where the dot represents the derivative with respect to z .

The implicit function theorem gives

$$\frac{\partial \Delta w_j(\mathbf{x}_0)}{\partial c(\mathbf{x}')} = - \frac{\partial \bar{f}_j / \partial c(\mathbf{x}')}{\partial \bar{f}_j / \partial \Delta w_j(\mathbf{x}_0)}, \quad (7)$$

where the denominator is given by

$$\frac{\partial \bar{f}_j}{\partial \Delta w_j(\mathbf{x}_0)} = \sum_{\mathbf{x} \in B(\mathbf{x}_0)} \ddot{m}_0(x, z + \Delta w_j(\mathbf{x}_0)) m_j(x, z). \quad (8)$$

Here the double dots represent the second-order derivative with respect to z .

Assuming only m_j is a function of the migration slowness, the numerator of equation 7 is

$$\frac{\partial \bar{f}_j}{\partial c(\mathbf{x}')} = \sum_{\mathbf{x} \in B(\mathbf{x}_0)} \dot{m}_0(x, z + \Delta w_j(\mathbf{x}_0)) \frac{\partial m_j(\mathbf{x})}{\partial c(\mathbf{x}')}.$$
 (9)

Inserting equations 7, 8 and 9 into equation 5 yields

$$\frac{\partial \epsilon}{\partial c(\mathbf{x}')} = \sum_{j=1}^{n_p} \sum_{\mathbf{x}_0 \in B} \frac{- \sum_{\mathbf{x} \in B(\mathbf{x}_0)} \Delta w_j(\mathbf{x}_0) \dot{m}_0(x, z + \Delta w_j(\mathbf{x}_0)) \frac{\partial m_j(\mathbf{x})}{\partial c(\mathbf{x}')}}{\sum_{\mathbf{x} \in B(\mathbf{x}_0)} \ddot{m}_0(x, z + \Delta w_j(\mathbf{x}_0)) m_j(\mathbf{x})}.$$
 (10)

Substituting the Fréchet derivative $\partial m_j(\mathbf{x})/\partial c(\mathbf{x}')$ derived in Appendix A into equation 10, the gradient of the objective function is

$$\frac{\partial \epsilon}{\partial c(\mathbf{x}')} = \sum_{j=1}^{n_p} \sum_{\mathbf{x}_0 \in B} \frac{\sum_{\mathbf{x} \in B(\mathbf{x}_0)} g_1 + g_2}{\sum_{\mathbf{x} \in B(\mathbf{x}_0)} \ddot{m}_0(x, z + \Delta w_j(\mathbf{x}_0)) m_j(\mathbf{x})},$$

where $g_1 = \Re \left\{ \sum_{\omega} 2\omega^2 c(\mathbf{x}') \bar{S}(\omega, \mathbf{x}') \left[\overbrace{G(\mathbf{x}'|\mathbf{x})^* \mathcal{M}(\mathbf{x}) \bar{R}(\omega, \mathbf{x})}^{\text{upward-propagated receiver wavefield}} \right]^* \right\},$ (11)

and $g_2 = \Re \left\{ \sum_{\omega} 2\omega^2 c(\mathbf{x}') \overbrace{G(\mathbf{x}'|\mathbf{x}) \mathcal{M}(\mathbf{x}) \bar{S}(\omega, \mathbf{x})}^{\text{upward-propagated source wavefield}} \bar{R}(\omega, \mathbf{x}')^* \right\},$

$$\text{in which } \mathcal{M}(\mathbf{x}) = -\Delta w_j(\mathbf{x}_0) \dot{m}_0(x, z + \Delta w_j(\mathbf{x}_0)).$$
 (12)

Here, $G(\mathbf{x}'|\mathbf{x})$ represents the Green's function recorded at \mathbf{x}' due to a harmonic point source at \mathbf{x} oscillating at a specific angular frequency ω . The gradient in equation 11 has two terms. The first term g_1 corresponds to the source-side wavepath, which is the dot product at \mathbf{x}' between the downward-propagated source-side wavefield $\bar{S}(\omega, \mathbf{x}')$ and the upward-propagated receiver-side wavefield. The upward propagated receiver-side wavefield

is generated by a virtual source at the image point \mathbf{x} , which is redatumed from the receivers at the surface as shown in Figure 1a. Similarly, the second term g_2 can be interpreted as the receiver-side wavepath, which is the dot product at \mathbf{x}' between the downward-propagated receiver-side wavefield $\bar{R}(\omega, \mathbf{x}')$ and the upward-propagated source-side wavefield. The upward propagated source-side wavefield is excited by a virtual source at the image point \mathbf{x} , which is redatumed from the sources at the surface as shown in Figure 1b. The migration slowness is updated by smearing the energy of the local image shifts at \mathbf{x} along its plane-wave paths associated with the sources and receivers as shown in Figure 1c.

The derivations from equations 4 to 12 are for the vertical shifts between 2D images. To be more general, the local shift between 3D images is a three-component vector, and the objective function in equation 4 can be generalized as the squared summation of the length of the shift vector. In this case, the corresponding gradient with respect to the migration slowness is derived in Appendix B.

Given the gradient, the steepest-descent method (Nocedal and Wright, 2006) can be used to iteratively update the migration slowness until the shifts in plane-wave CIGs are sufficiently small. An alternative is the conjugate gradient method (Nocedal and Wright, 2006) which is typically much faster than the steepest-descent method.

WORK FLOW

This section describes the workflow of the PWEMVA method, which is summarized into 3 steps: calculate the objective function, the gradient, and the step length. The implementations of the first two steps are described in detail.

1. Calculate the objective function

First, the shot profile seismic data are transformed into plane-wave gathers based on equation 2. Then plane-wave prestack reverse time migration (RTM) is applied to each plane-wave gather to obtain plane-wave CIGs. The poorly illuminated boundary areas of the migration images are masked.

The objective function in equation 4 requires calculating the local shifts between the same event in a plane-wave migration image and a reference image. In practice, the reference image is assumed to be the plane-wave migration image with $p = 0$, because it usually suffers the least from velocity errors.

We use semblance analysis method to calculate the shifts in the plane-wave CIGs. The semblance spectrum is calculated by scanning over different curvatures α of a parabola to fit the plane-wave CIGs:

$$\Delta\tilde{w}_j(\mathbf{x}) = \alpha p^2, \quad (13)$$

where $\Delta\tilde{w}_j(x, z)$ is the local shift which aligns $m_0(x, z)$ with $m_j(x, z + \Delta\tilde{w}_j(x, z))$. $\Delta\tilde{w}_j(x, z)$ can then be transformed into $\Delta w_j(x, z)$ by

$$\Delta w_j(x, z) = -\Delta\tilde{w}_j(x, z - \Delta\tilde{w}_j(x, z)). \quad (14)$$

The reason for fitting the plane-wave CIG with a parabola is explained in Appendix C. However, equation 13 implicitly assumes the apex of the parabola at the image with $p = 0$, and this is not accurate for a large dip-angle interface. In such case,

equation 13 is replaced with

$$\Delta\tilde{w}_j(\mathbf{x}) = \alpha(p - p_0)^2, \quad (15)$$

where $p_0 = \sin \beta / v(\mathbf{x})$.

Here p_0 is the ray parameter of the plane-wave reflecting off the interface with a dipping angle β perpendicularly and $v(\mathbf{x})$ is the migration velocity at \mathbf{x} . β can be computed from the migration image.

After calculating the semblance spectrum, the curvature corresponding to the maximum energy is automatically picked using the method proposed by Fomel (2009). As an example, Figure 2a shows a semblance spectrum computed from a plane-wave CIG shown in Figure 2b and the picked curvature parameters are then transformed into the shift based on equations 13 or 15 as shown in Figure 2c.

2. Calculate the gradient

When calculating the gradient in practice, equation 12 is simplified as

$$\mathcal{M}(\mathbf{x}) = -\Delta w_j(\mathbf{x}_0) \dot{m}_j(\mathbf{x}), \quad (16)$$

by assuming $\dot{m}_0(x, z + \Delta w_j(\mathbf{x}_0)) \approx \dot{m}_j(x, z)$. The denominator of equation 11 is also omitted in implementation because dividing an image can be unstable.

The Green's functions in equation 11 are computed by solving the two-way acoustic wave equation in the time domain while the background slowness model needs to be smoothed to avoid reflection events in the Green's functions. Given the gradient, a numerical line search method is used to calculate the step length and update the slowness model by the steepest-descent or the conjugate gradient method (Nocedal

and Wright, 2006).

NUMERICAL RESULTS

The PWEMVA method is applied to two synthetic datasets and a marine dataset recorded in the Gulf of Mexico. These tests are designed to demonstrate the strengths and limitations of this velocity analysis method.

Synthetic test 1

PWEMVA method is first tested on the data generated from a simple 2D model, which is 2 km wide and 0.5 km deep. Synthetic shot gathers are computed by finite-difference solutions to the 2D acoustic wave equation for the velocity model shown in Figure 3a. The source wavelet is a Ricker wavelet with a 40-Hz peak frequency, and there are 201 shots with 402 active receivers per shot. The sources and receivers are evenly distributed on the surface with an interval of 10 m and 5 m, respectively. The shot profile data are transformed into 41 plane-wave gathers with $-0.471 \text{ s/km} \leq p \leq 0.471 \text{ s/km}$ and shooting angles changing from -45 to 45 degrees. The plane-wave gather with $p = 0$ is shown in Figure 3b, and the initial velocity model is homogeneous with $v = 1.5 \text{ km/s}$. These CIGs using the initial velocity model are shown in Figure 4a. The semblance spectra and the moveout residuals computed from the CIGs at two locations are shown in Figures 4b and 4c. The inverted velocity models after 10 and 20 iterations are shown in Figures 5a and 5b, respectively, where the final tomogram accurately resembles the true velocity model. Figure 5c depicts the objective function at each iteration, and the plane-wave CIGs shown in Figure 6 are mostly flattened using the inverted velocity model after 20 iterations.

Synthetic test 2

The second test inverts the synthetic data generated by a staggered-grid acoustic modeling algorithm. The velocity and density models are shown in Figure 7 with the width of 21 km and the depth of 7.9 km taken from a portion of the BP2004 model. The source wavelet is a Ricker wavelet with a 15-Hz peak frequency. There are 690 shots with 2070 receivers per shot. The shots and receivers are evenly distributed on the surface at 30 m and 10 m intervals, respectively. These data are transformed into 81 plane-wave gathers with the ray parameters ranging from -0.33 s/km to 0.33 s/km and the shooting angles varying from -30 to 30 degrees. The laterally homogeneous velocity model shown in Figure 8a is the initial velocity, which produces the plane-wave CIGs with strong residual moveouts between 2 km to 8 km and 12.5 km to 15.5 km along the horizontal distance as shown in Figure 8b. Figure 9 depicts the semblance spectra and the picked curvatures at different horizontal locations. During the inversion, the water-layer around 100 meters deep is fixed.

The inverted velocity models after 5 and 10 iterations are shown in Figures 10a and 10b, respectively. After 10 iterations, the tomogram recovers most of the low wavenumber components of the true velocity model in Figure 7a. Figure 10c shows the objective function at each iteration, and the plane-wave CIGs associated with the inverted velocity after 10 iterations are mostly flattened as shown in Figure 11.

Field data test

The third example is for a 2D marine data set recorded in the Gulf of Mexico. The streamer data consist of 496 shots with a shot interval of 37.5 m. Each shot has 480 hydrophones with a receiver interval of 12.5 m. The maximum source-receiver offset is approximately

6 km, the nearest offset is 198 m, and the recording time is 5 seconds. Figure 12a shows a recorded common shot gather (CSG), where the 496 shot gathers are transformed into common midpoint profiles (CMPs) and a 2D spline interpolation is used to fill in the near-offset trace gap after normal moveout correction (Yilmaz, 2001). The interpolated CMPs are then transformed into common receiver gathers (CRGs) with a split-spread acquisition geometry using reciprocity (Liu et al., 2004). In the CRGs, each trace is multiplied by $\sqrt{i/\omega}$ in the frequency domain and then scaled by \sqrt{t} in the time domain to correct for the 3D geometrical spreading (Dai, 2012). A tau-p transform is applied to each CRG to generate 51 plane-wave gathers with $-0.33 \text{ s/km} \leq p \leq 0.33 \text{ s/km}$. The shooting angles vary from -30 to 30 degrees, and a plane-wave gather is shown in Figure 12b. The plane-wave gathers are filtered with a Wiener filter to transform the original wavelet to a Ricker wavelet with a 25-Hz peak frequency.

The initial velocity model shown in Figure 13a is obtained by inverting the traveltimes of the first arrivals. The plane-wave CIGs calculated by plane-wave RTM are shown in Figure 13b, with significant residual moveouts below 2 km and between 1 km to 9 km along the horizontal axis. The semblance analysis of the plane-wave CIGs illustrated in Figure 14 is used to calculate the spatial shifts for the migration image. After 10 iterations, the inverted velocity model is shown in Figure 15a, which produces the plane-wave CIGs shown in Figure 15b, with more flattened events especially below 2 km and between 1 to 9 km along the horizontal distance.

We now compare the shot profile RTM images from the initial and the inverted velocities, as shown in Figures 16a and 16b, respectively. The magnified views of the two images are compared in Figure 17. The comparison clearly shows that the RTM image using the inverted velocity model is better focused than that using the traveltime tomogram. Figures

18a and 18b show the angle-domain CIGs calculated by the method proposed by Sava and Fomel (2003) using the traveltime tomogram and the inverted velocity model, respectively. The angle-domain CIGs associated with the inverted velocity model have more flattened events, especially in the region surrounded by the red and yellow dashed squares in Figure 18. The magnified views of these two regions are compared in Figure 19.

DISCUSSIONS

In this section we discuss three issues which require attention for implementing the PWEMVA method. The first issue is the range of shooting angles and the number of plane waves. The second issue is the PWEMVA performance with a time-domain two-way wave equation compared to that with a one-way equation in the frequency domain. The third topic is the limitations of the PWEMVA method.

The maximum shooting angle α_2 for a plane wave usually ranges between 30 to 45 degree. The shooting angle does not need to be too large, since the velocity of the real earth typically increases with depth, so that a large shooting angle will reach a critical angle at certain shallow depths and fail to penetrate below. On the other hand, if the maximum shooting angle is too small, plane-wave CIGs will not have sufficient moveout information for the inversion. The minimum shooting angle α_1 is the negative of the maximum shooting angle. After determining the maximum and minimum shooting angles, the number of plane waves will determine the efficiency of the PWEMVA method. Zhang et al. (2005) state that the number of plane waves N_p must satisfy the constraint

$$N_p \geq \frac{L_s f (\sin \alpha_2 - \sin \alpha_1)}{v_s}, \quad (17)$$

where L_s is the length of a CRG and f is the frequency. This criterion ensures that the stacked plane-wave image is similar to a common-shot migration image. Since the PWEMVA method does not involve stacking, the required number of plane waves is fewer than N_p and can be decided by a trial-and-error procedure. An oversampled number of plane waves is inefficient while an undersampled number will generate significant aliasing artifacts in the CIGs.

In this paper, we migrate the plane-wave gathers and calculate the Green's functions by solving the two-way wave equation in the time domain. The alternative implementation is to solve the one-way wave equation in the frequency domain. The time-domain method is more accurate, yet requires more computational resources. This problem is more severe for surveys with a large source-receiver offset because, when computing a plane-wave gather, the delay time of a shot gather with a source at $(x_s, 0)$ is equal to $p * (x_s - x_0)$. This means that the longer source-receiver offset in a CRG, the longer the delay time, so that more computation time is required for the time-domain method. On the other hand, a frequency-domain implementation is immune to this problem, hence it is much faster than the time-domain method. However, solving the one-way wave equation in the frequency domain is an approximation to the two-way wave equation so that it is less accurate.

One disadvantage of the PWEMVA method is the artifacts in the plane-wave CIGs. Each trace in a CIG is computed by prestack plane-wave migration, thus it suffers from less signal-to-noise ratio and more cross-talk artifacts compared to traces in the angle domain, subsurface offset or time-lag CIGs, which is the result from stacking across all the shots. These artifacts in the plane-wave CIGs might bias the extraction of the moveout information. Another disadvantage is that the plane-wave gathers calculated from the CSGs with sparse source distribution are usually aliased. This problem is more severe in the cross-line

direction when extending the PWEMVA method to 3D velocity inversion. To mitigate this problem, CSGs need to be interpolated first and then transformed into plane-wave gathers as the data processing procedure applied to the Gulf of Mexico marine data set.

CONCLUSIONS

A WEMVA method using plane-wave CIGs is presented which reduces the computational cost and memory storage space, compared to the MVA analysis of CIGs in angle, subsurface-offset and time-lag domains. These benefits result from the following two properties. First, plane-wave CIGs are the direct output of prestack plane-wave migration, which does not require an imaging condition in the extended dimension or extra processing of the extrapolated wavefields during migration. Second, the number of plane waves is significantly fewer than the number of shots. In the second numerical test and the field data example, the number of plane waves is only approximately 10 percent of the number of shots, so that in these cases PWEMVA saves at least 90 percent of the computational time compared to other types of WEMVA method. The performance of the PWEMVA method largely depends on the quality of the plane-wave CIGs, thus the disadvantage of this method is that the artifacts in the plane-wave CIGs might bias the computation of the moveout information. One future work direction is to extend the PWEMVA method to 3D cases.

ACKNOWLEDGEMENTS

This research is supported by King Abdullah University of Science and Technology (KAUST) in Thuwal, Saudi Arabia. We are grateful to the sponsors of the Center for Subsurface Imaging and Fluid Modeling (CSIM) Consortium for their financial support. The first author

would like to thank Dr. Yunsong Huang for computing the travelttime tomogram of the field marine data. We also thank the Supercomputing Laboratory at KAUST for providing the computational resources required for carrying out this work.

APPENDIX A

DERIVATION OF THE MIGRATION IMAGE CHANGE WITH RESPECT TO THE MIGRATION SLOWNESS PERTURBATION

Based on the plane-wave migration imaging condition in equation 3, the Fréchet derivative of the image at \mathbf{x} with respect to the slowness perturbation at \mathbf{x}' consists of two terms:

$$\frac{\partial m(\mathbf{x})}{\partial c(\mathbf{x}')} = \overbrace{\Re\left\{\sum_{\omega} \frac{\partial \bar{S}(\omega, \mathbf{x})}{\partial c(\mathbf{x}')} \bar{R}(\omega, \mathbf{x})^*\right\}}^{\gamma_1} + \overbrace{\Re\left\{\sum_{\omega} \frac{\partial \bar{R}(\omega, \mathbf{x})^*}{\partial c(\mathbf{x}')} \bar{S}(\omega, \mathbf{x})\right\}}^{\gamma_2}, \quad (\text{A-1})$$

where the subscript j representing the plane-wave index is silent.

To derive the formula for γ_1 , we note that equation 1 leads to

$$\frac{\partial \bar{S}(\omega, \mathbf{x})}{\partial c(\mathbf{x}')} = \sum_{k=1}^{n_s} e^{i\omega p(x_k - x_0)} \frac{\partial S_k(\omega, \mathbf{x})}{\partial c(\mathbf{x}')}.$$
(A-2)

The wavefield $S_k(\omega, \mathbf{x})$ is initiated by a point source located at $\mathbf{x}_k = (x_k, 0)$ at the surface and is defined as

$$S_k(\omega, \mathbf{x}) = G(\mathbf{x}|\mathbf{x}_k)W(\omega), \quad (\text{A-3})$$

where $G(\mathbf{x}|\mathbf{x}_k)$ represents the Green's function recorded at \mathbf{x} due to a harmonic point source at \mathbf{x}_k , and $W(\omega)$ represents the source spectrum. Here, we assume the source is zero phase.

Inserting equation A-3 into equation A-2 leads to

$$\frac{\partial \bar{S}(\omega, \mathbf{x})}{\partial c(\mathbf{x}')} = \sum_{k=1}^{n_s} e^{i\omega p(x_k - x_0)} \frac{\partial G(\mathbf{x}|\mathbf{x}_k)}{\partial c(\mathbf{x}')} W(\omega). \quad (\text{A-4})$$

The perturbed Green's function $\Delta G(\mathbf{x}|\mathbf{x}_k)$ can be expressed under the Born approximation as

$$\Delta G(\mathbf{x}|\mathbf{x}_k) = \int 2\omega^2 c(\mathbf{x}'') G(\mathbf{x}|\mathbf{x}'') G(\mathbf{x}''|\mathbf{x}_k) \Delta c(\mathbf{x}'') d\mathbf{x}'', \quad (\text{A-5})$$

where $\Delta c(\mathbf{x}'')$ is the slowness perturbation. Assuming

$$\Delta c(\mathbf{x}'') = \Delta c \delta(\mathbf{x}'' - \mathbf{x}'), \quad (\text{A-6})$$

we obtain

$$\frac{\partial G(\mathbf{x}, \mathbf{x}_k)}{\partial c(\mathbf{x}')} = 2\omega^2 c(\mathbf{x}') G(\mathbf{x}|\mathbf{x}') G(\mathbf{x}'|\mathbf{x}_k). \quad (\text{A-7})$$

Substituting the combination of equations A-4 and A-7 into the expression of γ_1 in equation A-1 yields

$$\gamma_1 = \Re \left\{ \sum_{\omega} 2\omega^2 c(\mathbf{x}') W(\omega) \sum_{k=1}^{n_s} e^{i\omega p(x_k - x_0)} G(\mathbf{x}'|\mathbf{x}_k) G(\mathbf{x}|\mathbf{x}') \bar{R}(\omega, \mathbf{x})^* \right\}. \quad (\text{A-8})$$

Inserting equations 1 and A-3 into equation A-8 and using the reciprocity property of the Green's function $G(\mathbf{x}|\mathbf{x}') = G(\mathbf{x}'|\mathbf{x})$, equation A-8 is simplified as

$$\gamma_1 = \Re \left\{ \sum_{\omega} 2\omega^2 c(\mathbf{x}') \bar{S}(\omega, \mathbf{x}') [G(\mathbf{x}'|\mathbf{x})^* \bar{R}(\omega, \mathbf{x})]^* \right\}. \quad (\text{A-9})$$

The formula for γ_2 is derived in a similar way. Based on equation 2

$$\frac{\partial \bar{R}(\omega, \mathbf{x})}{\partial c(\mathbf{x}')} = \sum_{k=1}^{n_s} e^{i\omega p(x_k - x_0)} \frac{\partial R_k(\omega, \mathbf{x})}{\partial c(\mathbf{x}')}, \quad (\text{A-10})$$

$$\text{and } R_k(\omega, \mathbf{x}) = \sum_{\mathbf{x}_g} G(\mathbf{x}|\mathbf{x}_g)^* d(\omega, \mathbf{x}_g, \mathbf{x}_k), \quad (\text{A-11})$$

where $R_k(\omega, \mathbf{x})$ is the backward extrapolated wavefield computed by the time-reversed propagation of the data $d(\omega, \mathbf{x}_g, \mathbf{x}_k)$ recorded at \mathbf{x}_g excited by the source at \mathbf{x}_k .

Similar to equation A-7, Born modeling gives

$$\frac{\partial G(\mathbf{x}, \mathbf{x}_g)}{\partial c(\mathbf{x}')} = 2\omega^2 c(\mathbf{x}') G(\mathbf{x}|\mathbf{x}') G(\mathbf{x}'|\mathbf{x}_g). \quad (\text{A-12})$$

Substituting equations A-11 and A-12 into equation A-10 gives

$$\begin{aligned} \frac{\partial \bar{R}(\omega, \mathbf{x})}{\partial c(\mathbf{x}')} &= \sum_{k=1}^{n_s} e^{i\omega p(x_k - x_0)} 2\omega^2 c(\mathbf{x}') G(\mathbf{x}|\mathbf{x}')^* \sum_{\mathbf{x}_g} G(\mathbf{x}'|\mathbf{x}_g)^* d(\omega, \mathbf{x}_g, \mathbf{x}_k), \\ &= 2\omega^2 c(\mathbf{x}') G(\mathbf{x}|\mathbf{x}')^* \bar{R}(\omega, \mathbf{x}'). \end{aligned} \quad (\text{A-13})$$

Inserting equation A-13 into the expression of γ_2 in equation A-1 and using the reciprocity property $G(\mathbf{x}|\mathbf{x}') = G(\mathbf{x}'|\mathbf{x})$ yields

$$\gamma_2 = \Re \left\{ \sum_{\omega} 2\omega^2 c(\mathbf{x}') [\bar{S}(\omega, \mathbf{x}) G(\mathbf{x}'|\mathbf{x})] \bar{R}(\omega, \mathbf{x}')^* \right\}. \quad (\text{A-14})$$

Summarizing the previous derivations, we have

$$\begin{aligned} \frac{\partial m(\mathbf{x})}{\partial c(\mathbf{x}')} &= \gamma_1 + \gamma_2, \\ \text{where } \gamma_1 &= \Re \left\{ \sum_{\omega} 2\omega^2 c(\mathbf{x}') \bar{S}(\omega, \mathbf{x}') [G(\mathbf{x}'|\mathbf{x})^* \bar{R}(\omega, \mathbf{x})]^* \right\}, \\ \text{and } \gamma_2 &= \Re \left\{ \sum_{\omega} 2\omega^2 c(\mathbf{x}') [\bar{S}(\omega, \mathbf{x}) G(\mathbf{x}'|\mathbf{x})] \bar{R}(\omega, \mathbf{x}')^* \right\}. \end{aligned} \quad (\text{A-15})$$

APPENDIX B

EXTENSION OF THE OBJECTIVE FUNCTION AND GRADIENT TO 3D CASES

The local shift between two small cubes $B(\mathbf{x}_0)$ centered at \mathbf{x}_0 of a 3D plane-wave migration image $m_j(\mathbf{x})$ and a reference image $m_0(\mathbf{x})$ is a three-component vector $\Delta \mathbf{u}_j(\mathbf{x}_0) = (\Delta u_j(\mathbf{x}_0), \Delta v_j(\mathbf{x}_0), \Delta w_j(\mathbf{x}_0))$, where Δu_j , Δv_j and Δw_j are the components in the x , y and z directions, respectively. Similar to equation 4, the objective function is defined as

$$\epsilon = \frac{1}{2} \sum_{j=1}^{n_p} \sum_{\mathbf{x}_0 \in B} \|\Delta \mathbf{u}_j(\mathbf{x}_0)\|^2, \quad (\text{B-1})$$

where $\|\cdot\|$ denotes the length of the vector. The local shift vector $\Delta \mathbf{u}_j(\mathbf{x}_0)$ aligns $m_0(\mathbf{x} + \Delta \mathbf{u}_j(\mathbf{x}_0))$ with $m_j(\mathbf{x})$ for $\mathbf{x} \in B(\mathbf{x}_0)$, where the size of $B(\mathbf{x}_0)$ is a wavelength. The gradient of the objective function with respect to the migration slowness $c(\mathbf{x}')$ is

$$\frac{\partial \epsilon}{\partial c(\mathbf{x}')} = \sum_{j=1}^{n_p} \sum_{\mathbf{x}_0 \in B} \left\{ \frac{\partial \Delta u_j(\mathbf{x}_0)}{\partial c(\mathbf{x}')} \Delta u_j(\mathbf{x}_0) + \frac{\partial \Delta v_j(\mathbf{x}_0)}{\partial c(\mathbf{x}')} \Delta v_j(\mathbf{x}_0) + \frac{\partial \Delta w_j(\mathbf{x}_0)}{\partial c(\mathbf{x}')} \Delta w_j(\mathbf{x}_0) \right\}. \quad (\text{B-2})$$

The connective function is defined as

$$f_j(c(\mathbf{x}'), \mathbf{u}_j(\mathbf{x}_0)) = \sum_{\mathbf{x} \in B(\mathbf{x}_0)} m_0(\mathbf{x} + \mathbf{u}_j(\mathbf{x}_0)) m_j(\mathbf{x}), \quad (\text{B-3})$$

where $\mathbf{u}_j(\mathbf{x}_0)$ is a random local shift vector. The correct image shift $\Delta \mathbf{u}_j(\mathbf{x}_0)$ aligns $m_0(\mathbf{x} + \Delta \mathbf{u}_j(\mathbf{x}_0))$ with $m_j(\mathbf{x})$. This means that the gradient of f_j with respect to $\mathbf{u}_j(\mathbf{x}_0)$ should be zero at $\Delta \mathbf{u}_j(\mathbf{x}_0)$:

$$\begin{aligned} \bar{f}_j(c(\mathbf{x}'), \Delta \mathbf{u}_j(\mathbf{x}_0)) &= \nabla f_j(c(\mathbf{x}'), \mathbf{u}_j(\mathbf{x}_0)) \Big|_{\mathbf{u}_j(\mathbf{x}_0) = \Delta \mathbf{u}_j(\mathbf{x}_0)} \\ &= (\bar{f}x_j, \bar{f}y_j, \bar{f}z_j) \\ &= \sum_{\mathbf{x} \in B(\mathbf{x}_0)} m_j(\mathbf{x}) \left(\frac{\partial m_0(\mathbf{x} + \Delta \mathbf{u}_j(\mathbf{x}_0))}{\partial x}, \frac{\partial m_0(\mathbf{x} + \Delta \mathbf{u}_j(\mathbf{x}_0))}{\partial y}, \frac{\partial m_0(\mathbf{x} + \Delta \mathbf{u}_j(\mathbf{x}_0))}{\partial z} \right) \\ &= (0, 0, 0) \end{aligned} \quad (\text{B-4})$$

From the implicit function theorem we have

$$\begin{pmatrix} \frac{\partial \Delta u_j(\mathbf{x}_0)}{\partial c(\mathbf{x}')} \\ \frac{\partial \Delta v_j(\mathbf{x}_0)}{\partial c(\mathbf{x}')} \\ \frac{\partial \Delta w_j(\mathbf{x}_0)}{\partial c(\mathbf{x}')} \end{pmatrix} = - \begin{pmatrix} \frac{\partial \bar{f}x_j}{\partial \Delta u_j(\mathbf{x}_0)} & \frac{\partial \bar{f}x_j}{\partial \Delta v_j(\mathbf{x}_0)} & \frac{\partial \bar{f}x_j}{\partial \Delta w_j(\mathbf{x}_0)} \\ \frac{\partial \bar{f}y_j}{\partial \Delta u_j(\mathbf{x}_0)} & \frac{\partial \bar{f}y_j}{\partial \Delta v_j(\mathbf{x}_0)} & \frac{\partial \bar{f}y_j}{\partial \Delta w_j(\mathbf{x}_0)} \\ \frac{\partial \bar{f}z_j}{\partial \Delta u_j(\mathbf{x}_0)} & \frac{\partial \bar{f}z_j}{\partial \Delta v_j(\mathbf{x}_0)} & \frac{\partial \bar{f}z_j}{\partial \Delta w_j(\mathbf{x}_0)} \end{pmatrix}^{-1} \begin{pmatrix} \frac{\partial \bar{f}x_j}{\partial c(\mathbf{x}')} \\ \frac{\partial \bar{f}y_j}{\partial c(\mathbf{x}')} \\ \frac{\partial \bar{f}z_j}{\partial c(\mathbf{x}')} \end{pmatrix} \quad (\text{B-5})$$

Inserting the expressions of $\overline{fx_j}$, $\overline{fy_j}$ and $\overline{fz_j}$ in equation B-4 into equation B-5 yields

$$\begin{pmatrix} \frac{\partial \Delta u_j(\mathbf{x}_0)}{\partial c(\mathbf{x}')} \\ \frac{\partial \Delta v_j(\mathbf{x}_0)}{\partial c(\mathbf{x}')} \\ \frac{\partial \Delta w_j(\mathbf{x}_0)}{\partial c(\mathbf{x}')} \end{pmatrix} = -A^{-1} \begin{pmatrix} \sum_{\mathbf{x} \in B(\mathbf{x}_0)} \frac{\partial m_j(\mathbf{x})}{\partial c(\mathbf{x}')} \frac{\partial m_0(\mathbf{x} + \Delta \mathbf{u}_j(\mathbf{x}_0))}{\partial x} \\ \sum_{\mathbf{x} \in B(\mathbf{x}_0)} \frac{\partial m_j(\mathbf{x})}{\partial c(\mathbf{x}')} \frac{\partial m_0(\mathbf{x} + \Delta \mathbf{u}_j(\mathbf{x}_0))}{\partial y} \\ \sum_{\mathbf{x} \in B(\mathbf{x}_0)} \frac{\partial m_j(\mathbf{x})}{\partial c(\mathbf{x}')} \frac{\partial m_0(\mathbf{x} + \Delta \mathbf{u}_j(\mathbf{x}_0))}{\partial z} \end{pmatrix}, \quad (\text{B-6})$$

where $A = \sum_{\mathbf{x} \in B(\mathbf{x}_0)} m_j(\mathbf{x}) \begin{pmatrix} \frac{\partial^2 m_0(\mathbf{x} + \Delta \mathbf{u}_j(\mathbf{x}_0))}{\partial x^2} & \frac{\partial^2 m_0(\mathbf{x} + \Delta \mathbf{u}_j(\mathbf{x}_0))}{\partial x \partial y} & \frac{\partial^2 m_0(\mathbf{x} + \Delta \mathbf{u}_j(\mathbf{x}_0))}{\partial x \partial z} \\ \frac{\partial^2 m_0(\mathbf{x} + \Delta \mathbf{u}_j(\mathbf{x}_0))}{\partial y \partial x} & \frac{\partial^2 m_0(\mathbf{x} + \Delta \mathbf{u}_j(\mathbf{x}_0))}{\partial y^2} & \frac{\partial^2 m_0(\mathbf{x} + \Delta \mathbf{u}_j(\mathbf{x}_0))}{\partial y \partial z} \\ \frac{\partial^2 m_0(\mathbf{x} + \Delta \mathbf{u}_j(\mathbf{x}_0))}{\partial z \partial x} & \frac{\partial^2 m_0(\mathbf{x} + \Delta \mathbf{u}_j(\mathbf{x}_0))}{\partial z \partial y} & \frac{\partial^2 m_0(\mathbf{x} + \Delta \mathbf{u}_j(\mathbf{x}_0))}{\partial z^2} \end{pmatrix}.$

Substituting equation B-6 into equation B-2 gives the gradient of the objective function in equation B-1.

APPENDIX C

MOVEOUT ANALYSIS OF PLANE-WAVE CIGS

For a stack of N horizontal layers, Jiao et al. (2002) shows that the migration image depth

$z_N^m(p)$ of the plane-wave gather with the ray parameter p is

$$z_N^m(p) = \sum_{i=1}^N \Delta z_i^t \frac{\sqrt{(c_i^t)^2 - p^2}}{\sqrt{(c_i^m)^2 - p^2}}, \quad (\text{C-1})$$

where c_i^t (c_i^m) represents the correct (incorrect) migration slowness at the i -th layer.

Using the Taylor expansion and truncating after the second term gives

$$\frac{\sqrt{(c_i^t)^2 - p^2}}{\sqrt{(c_i^m)^2 - p^2}} \approx \alpha_i^{(0)} + \alpha_i^{(2)} p^2, \quad (\text{C-2})$$

where

$$\begin{aligned} \alpha_i^{(0)} &= c_i^t / c_i^m, \\ \alpha_i^{(2)} &= \frac{1}{2(c_i^m)^2} \left(\frac{c_i^t}{c_i^m} - \frac{c_i^m}{c_i^t} \right). \end{aligned} \quad (\text{C-3})$$

Substituting equation C-2 into equation C-1 yields

$$z_N^m(p) \approx \sum_{i=1}^N \Delta z_i^t \left(\alpha_i^{(0)} + \alpha_i^{(2)} p^2 \right). \quad (\text{C-4})$$

Based on equation C-4, the depth shift between the plane-wave migration images with ray parameters of p and 0 is

$$z_N^m(p) - z_N^m(p=0) = \left(\sum_{i=1}^N \alpha_i^{(2)} \right) p^2, \quad (\text{C-5})$$

which suggests that the moveout of the plane-wave CIG can be approximated by a parabola.

REFERENCES

- Biondi, B., P. Sava, et al., 1999, Wave-equation migration velocity analysis: SEG Technical Program Expanded Abstracts 1999, 1723–1726.
- Biondi, B. and W. W. Symes, 2004, Angle-domain common-image gathers for migration velocity analysis by wavefield-continuation imaging: *Geophysics*, **69**, 1283–1298.
- Dai, W., 2012, Multisource least-squares migration and prism wave reverse time migration: PhD thesis, The University of Utah.
- Dai, W. and G. T. Schuster, 2013, Plane-wave least-squares reverse-time migration: *Geophysics*, **78**, S165–S177.
- Dickens, T. A. and G. A. Winbow, 2011, RTM angle gathers using poynting vectors: SEG Technical Program Expanded Abstracts 2011, 3109–3113.
- Duquet, B., P. Lailly, and A. Ehinger, 2001, 3D plane wave migration of streamer data: SEG Technical Program Expanded Abstracts 2001, 1033–1036.
- Fomel, S., 2009, Velocity analysis using ab semblance: *Geophysical Prospecting*, **57**, 311–321.
- Jiao, J., P. L. Stoffa, M. K. Sen, and R. K. Seifoullaev, 2002, Residual migration-velocity analysis in the plane-wave domain: *Geophysics*, **67**, 1258–1269.
- Liu, F., D. W. Hanson, N. D. Whitmore, R. S. Day, and R. H. Stolt, 2006, Toward a unified analysis for source plane-wave migration: *Geophysics*, **71**, S129–S139.
- Liu, F., D. N. Whitmore, D. W. Hanson, R. S. Day, C. C. Mosher, et al., 2004, The impact of reciprocity on prestack source plane wave migration: Presented at the 2004 SEG Annual Meeting.
- Luo, Y. and G. T. Schuster, 1991, Wave-equation travelttime inversion: *Geophysics*, **56**, 645–653.

- Mulder, W. and A. Ten Kroode, 2002, Automatic velocity analysis by differential semblance optimization: *Geophysics*, **67**, 1184–1191.
- Nocedal, J. and S. Wright, 2006, *Numerical optimization*: Springer Science & Business Media.
- Rickett, J. E. and P. C. Sava, 2002, Offset and angle-domain common image-point gathers for shot-profile migration: *Geophysics*, **67**, 883–889.
- Sava, P. and B. Biondi, 2004, Wave-equation migration velocity analysis. i. theory: *Geophysical Prospecting*, **52**, 593–606.
- Sava, P. and S. Fomel, 2006, Time-shift imaging condition in seismic migration: *Geophysics*, **71**, S209–S217.
- Sava, P. C. and S. Fomel, 2003, Angle-domain common-image gathers by wavefield continuation methods: *Geophysics*, **68**, 1065–1074.
- Shen, P. and W. W. Symes, 2008, Automatic velocity analysis via shot profile migration: *Geophysics*, **73**, VE49–VE59.
- Vigh, D. and E. W. Starr, 2008, 3D prestack plane-wave full-waveform inversion: *Geophysics*, **73**, VE135–VE144.
- Wang, X., W. Dai, Y. Huang, and G. T. Schuster, 2014, 3D plane-wave least-squares kirchhoff migration: *SEG Technical Program Expanded Abstracts 2014*, 3974–3979.
- Whitmore, N. D., 1995, *An imaging hierarchy for common-angle plane wave seismograms*: PhD thesis, University of Tulsa.
- Xu, S., H. Chauris, G. Lambar, and M. Noble, 2001, Common angle migration: A strategy for imaging complex media: *Geophysics*, **66**, 1877–1894.
- Xu, S., Y. Zhang, and B. Tang, 2011, 3D angle gathers from reverse time migration: *Geophysics*, **76**, S77–S92.

- Yilmaz, Ö., 2001, Seismic data analysis, volume 1: Society of exploration geophysicists
Tulsa, OK.
- Zhang, Q., 2014, RTM angle gathers and specular filter (SF) RTM using optical flow: SEG
Technical Program Expanded Abstracts 2014, 3816–3820.
- Zhang, S., Y. Luo, and G. Schuster, 2015, Shot- and angle-domain wave-equation travelttime
inversion of reflection data: Theory: Geophysics, **80**, U47–U59.
- Zhang, Y. and B. Biondi, 2013, Moveout-based wave-equation migration velocity analysis:
Geophysics, **78**, U31–U39.
- Zhang, Y., J. Sun, C. Notfors, S. H. Gray, L. Chernis, and J. Young, 2005, Delayed-shot
3D depth migration: Geophysics, **70**, E21–E28.

LIST OF FIGURES

1 Wavepath diagrams illustrate (a) g_1 , (b) g_2 and (c) $g_1 + g_2$, where $\mathcal{M}(\mathbf{x})$ is an interface of a positive value as shown by the black horizontal line in panels (a) and (b).

2 (a) A semblance spectrum calculated from (b) a plane-wave CIG. (c) The vertical shift of the CIG calculated from the picked curvature parameters in panel (a). The data are generated for a laterally homogeneous 6-layer velocity model, and then migrated using a homogeneous velocity slower than the true velocity. The curvature parameters corresponding to the maximum energy of the spectrum are picked automatically as shown by the red line in panel a, and then transformed into the shift values in panel c. The dashed red lines in panel b represent the depth calculated from the shift values, which match well with the depths of the migrated events.

3 (a) True velocity model and (b) the plane-wave gather with $p = 0$.

4 (a) Plane-wave CIGs migrated using a homogeneous velocity model. The calculated semblance spectra and the picked curvatures at 0.75 km and 1 km are shown in (b) and (c).

5 (a) Inverted velocity after 10 iterations and (b) 20 iterations. (c) The objective function at each iteration.

6 Plane-wave CIGs using the inverted velocity model shown in Figure 5b.

7 (a) True velocity model and (b) true density model.

8 (a) Initial velocity model and (b) the associated plane-wave CIGs.

9 Semblance spectra at (a) $x = 3.5$ km, (b) $x = 6.5$ km, (c) $x = 9.5$ km, (d) $x = 12.5$ km and (e) $x = 15.5$ km. The red lines represent the picked curvatures of the maximum energy.

10 Inverted velocity model after (a) 5 iterations and (b) 10 iterations. Panel (c) shows

the objective function at each iteration.

11 Plane-wave CIGs using the inverted velocity model shown in Figure 10b.

12 (a) A CSG recorded in the Gulf of Mexico data and (b) a plane-wave gather with $p = -0.04$ s/km.

13 (a) The initial velocity model computed by inverting the traveltimes of the first arrivals and (b) the associated plane-wave CIGs.

14 Plane-wave CIGs are used to calculate the semblance spectra and the shifts of CIGs.

15 (a) The inverted velocity model after 10 iterations and (b) the associated plane-wave CIGs.

16 Shot profile RTM images based on the (a) traveltime tomogram in Figure 13a and (b) inverted velocity model shown in Figure 15a.

17 (a), (c), and (e) are the zoom-in view of the red, green and the yellow squares in Figure 16a, respectively. (b), (d), and (f) are the zoom-in view of the red, green and the yellow squares in Figure 16b, respectively.

18 Angle-domain CIGs calculated from the (a) traveltime tomogram in Figure 13a and (b) inverted velocity shown in Figure 15a.

19 (a) and (c) are the zoom-in view of the red and the green squares in Figure 18a. (b) and (d) are the zoom-in view of the red and the green squares in Figure 18b.

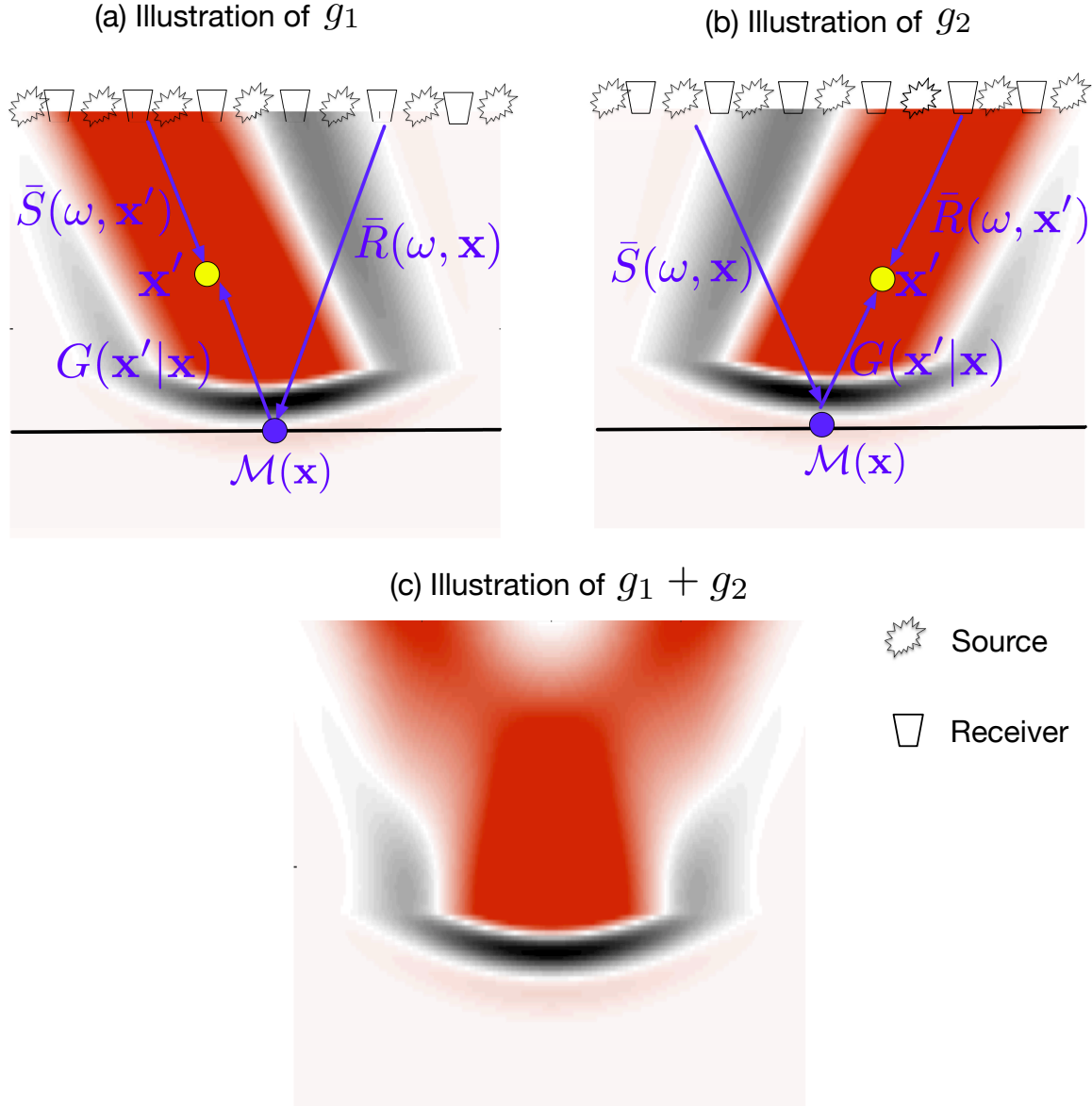


Figure 1: Wavepath diagrams illustrate (a) g_1 , (b) g_2 and (c) $g_1 + g_2$, where $\mathcal{M}(\mathbf{x})$ is an interface of a positive value as shown by the black horizontal line in panels (a) and (b).

Guo & Schuster –

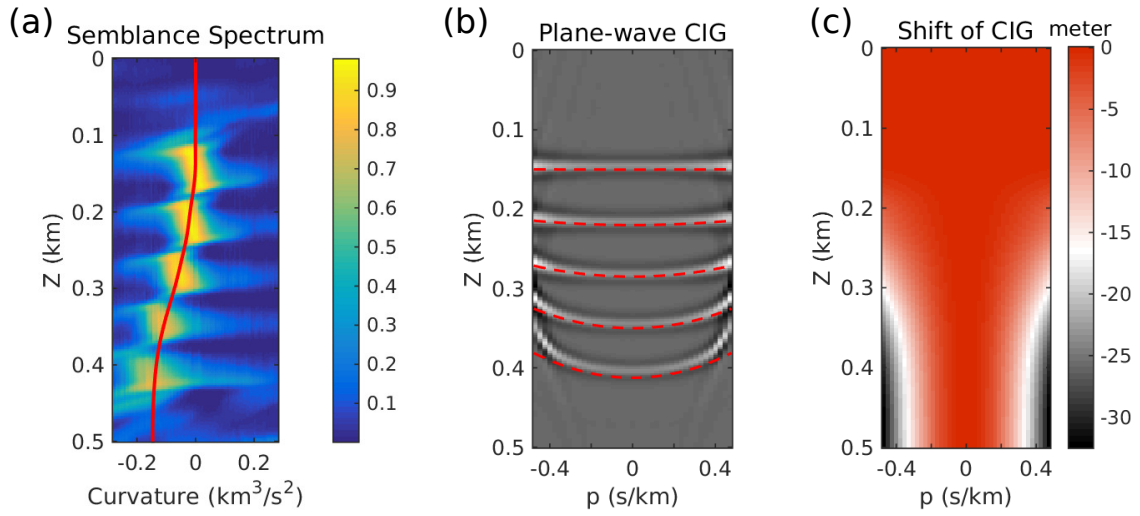


Figure 2: (a) A semblance spectrum calculated from (b) a plane-wave CIG. (c) The vertical shift of the CIG calculated from the picked curvature parameters in panel (a). The data are generated for a laterally homogeneous 6-layer velocity model, and then migrated using a homogeneous velocity slower than the true velocity. The curvature parameters corresponding to the maximum energy of the spectrum are picked automatically as shown by the red line in panel a, and then transformed into the shift values in panel c. The dashed red lines in panel b represent the depth calculated from the shift values, which match well with the depths of the migrated events.

Guo & Schuster –

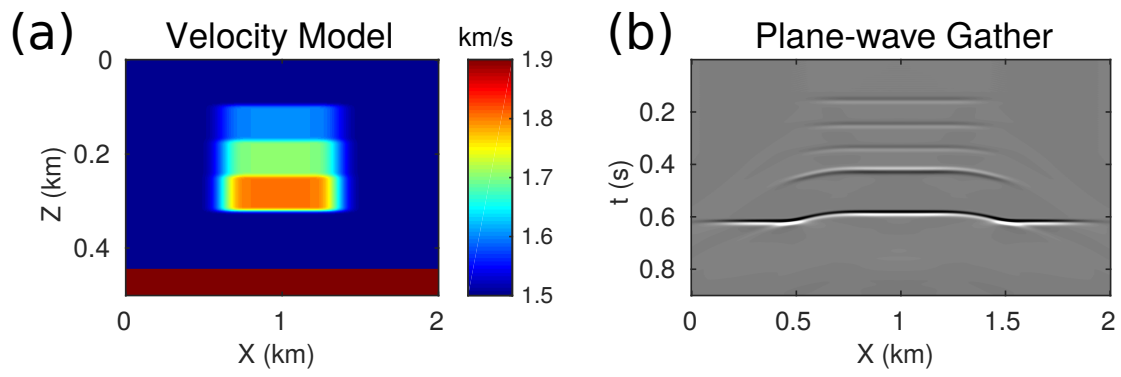


Figure 3: (a) True velocity model and (b) the plane-wave gather with $p = 0$.
Guo & Schuster –

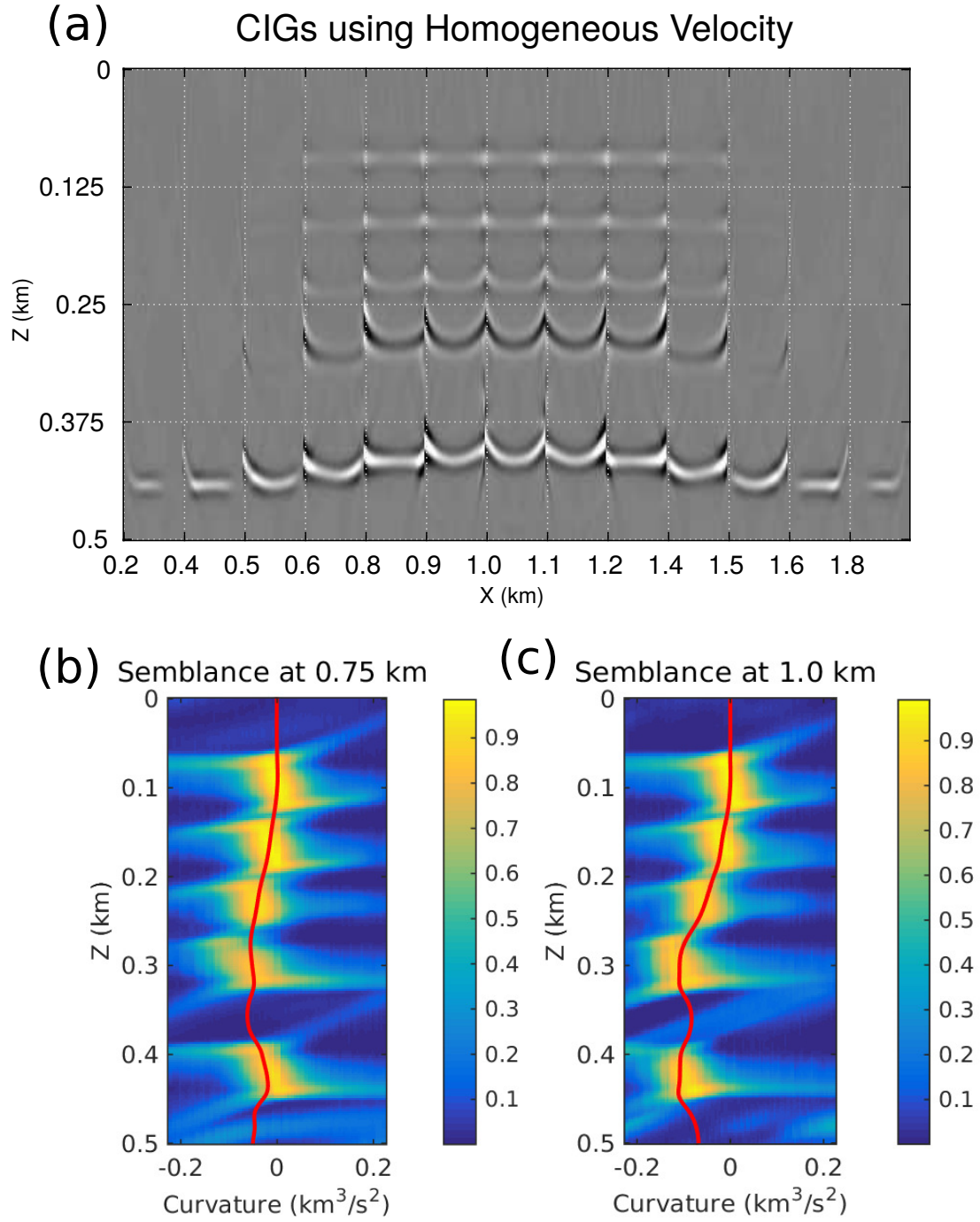


Figure 4: (a) Plane-wave CIGs migrated using a homogeneous velocity model. The calculated semblance spectra and the picked curvatures at 0.75 km and 1 km are shown in (b) and (c).

Guo & Schuster –

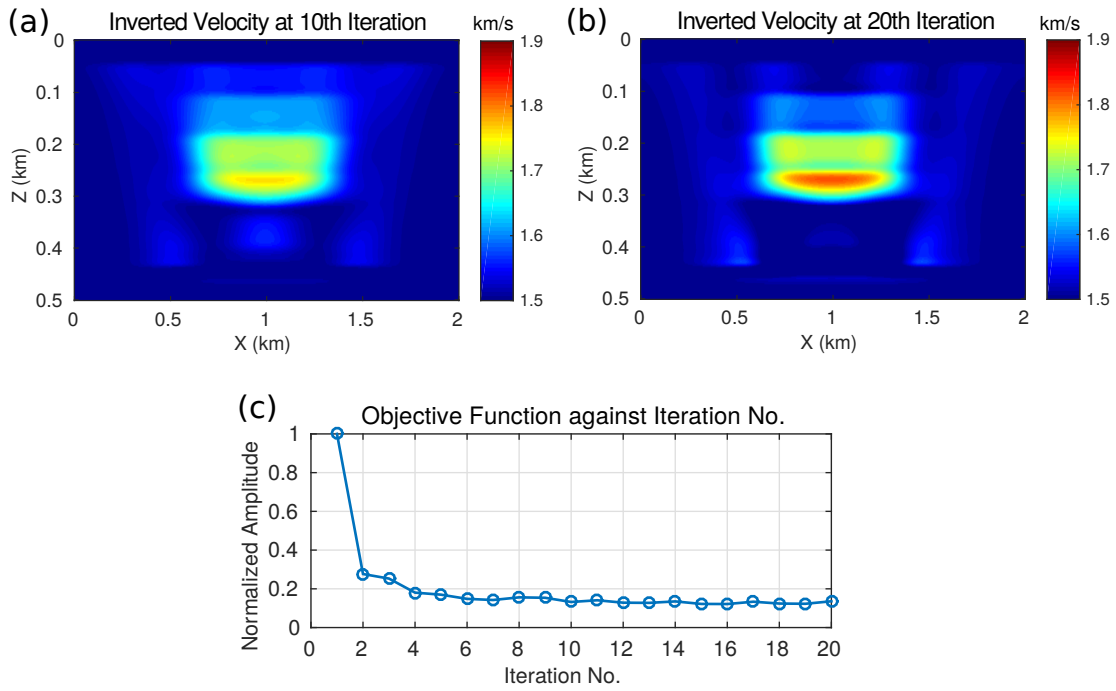


Figure 5: (a) Inverted velocity after 10 iterations and (b) 20 iterations. (c) The objective function at each iteration.

Guo & Schuster –

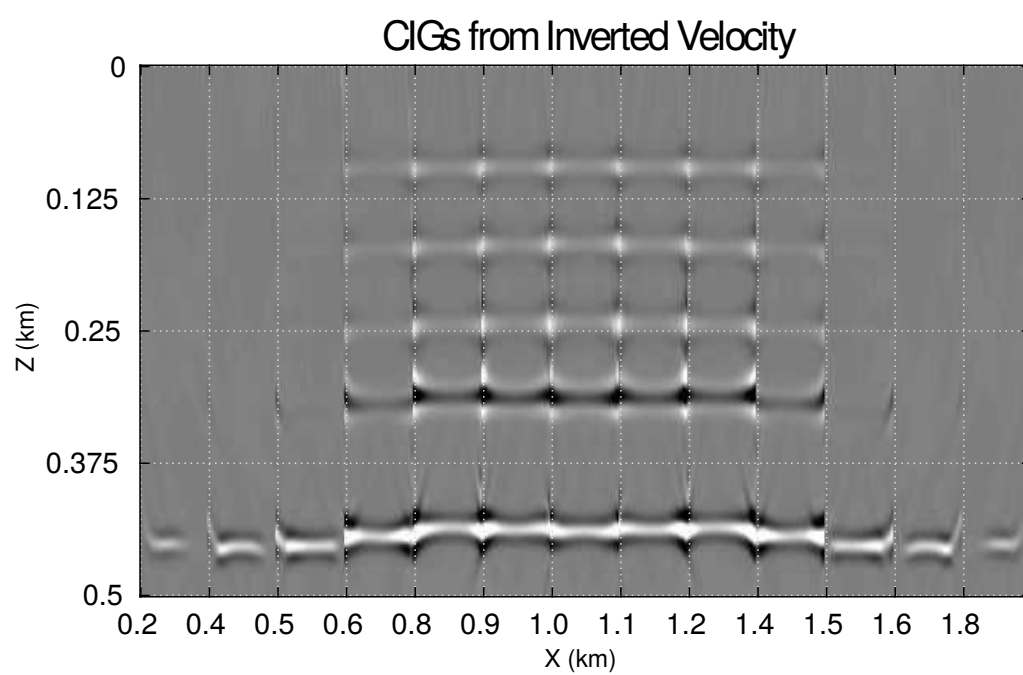


Figure 6: Plane-wave CIGs using the inverted velocity model shown in Figure 5b.
Guo & Schuster –

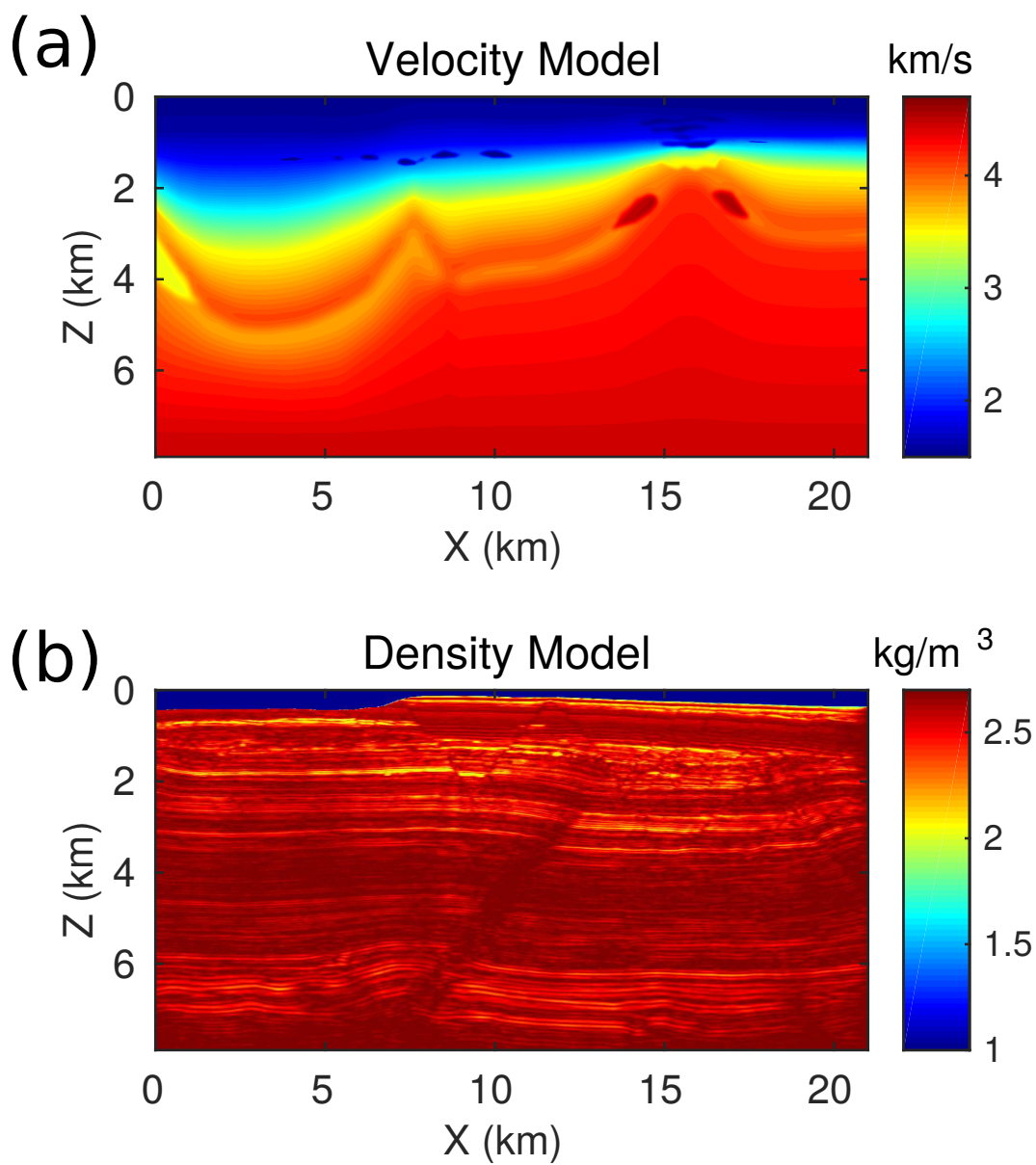


Figure 7: (a) True velocity model and (b) true density model. **Guo & Schuster** –

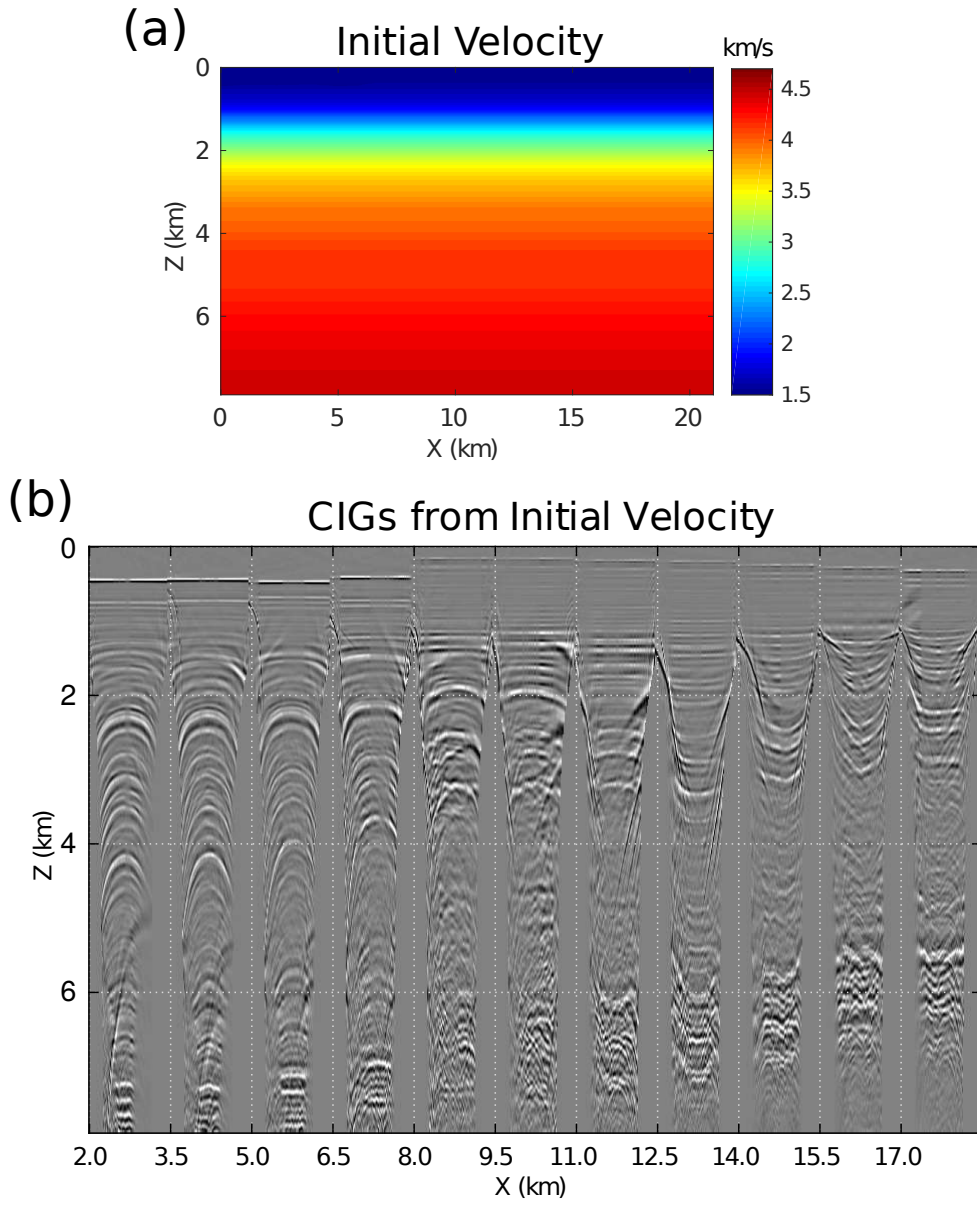


Figure 8: (a) Initial velocity model and (b) the associated plane-wave CIGs.
Guo & Schuster –

Semblance Spectra

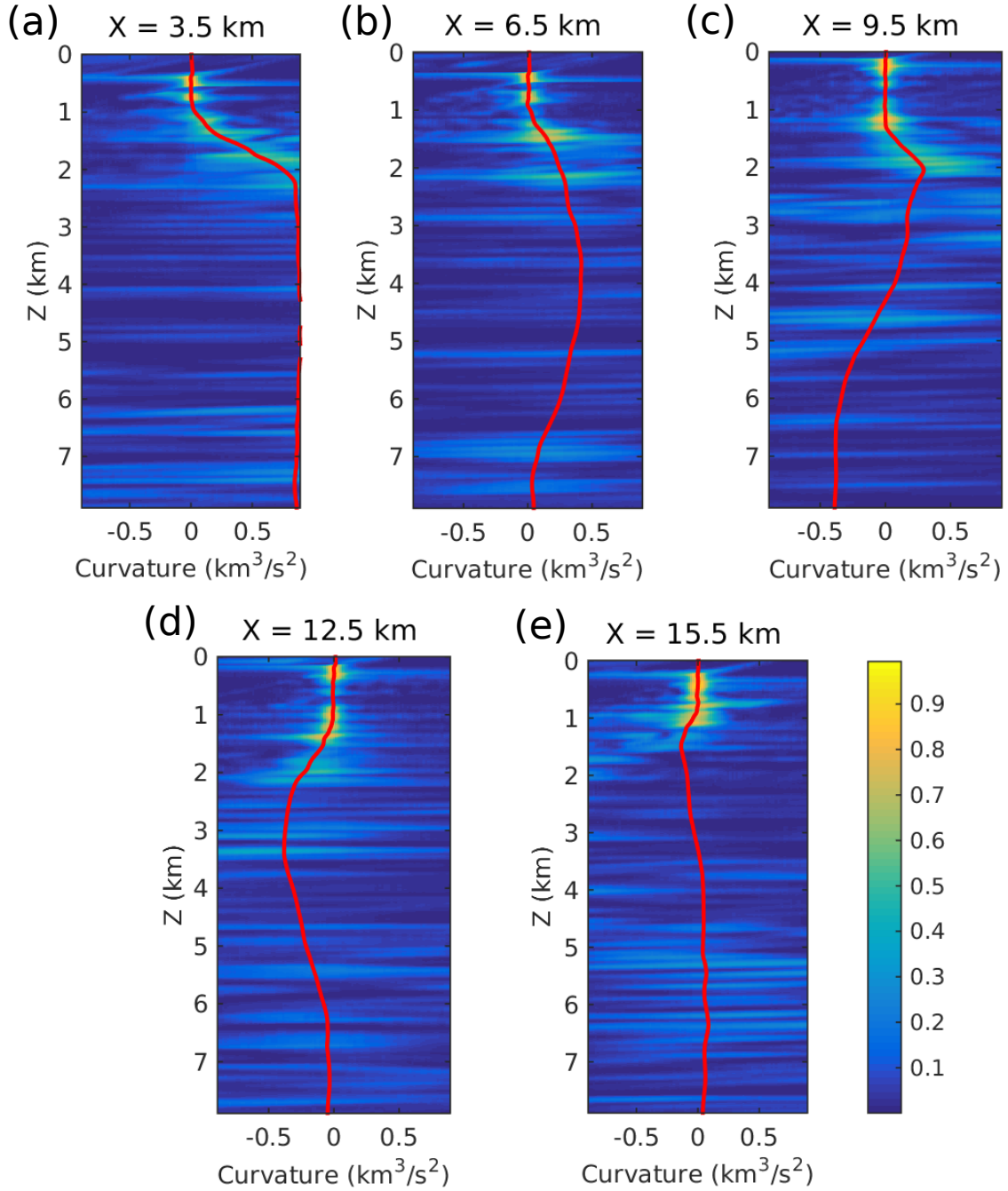


Figure 9: Semblance spectra at (a) $x = 3.5$ km, (b) $x = 6.5$ km, (c) $x = 9.5$ km, (d) $x = 12.5$ km and (e) $x = 15.5$ km. The red lines represent the picked curvatures of the maximum energy.

Guo & Schuster –

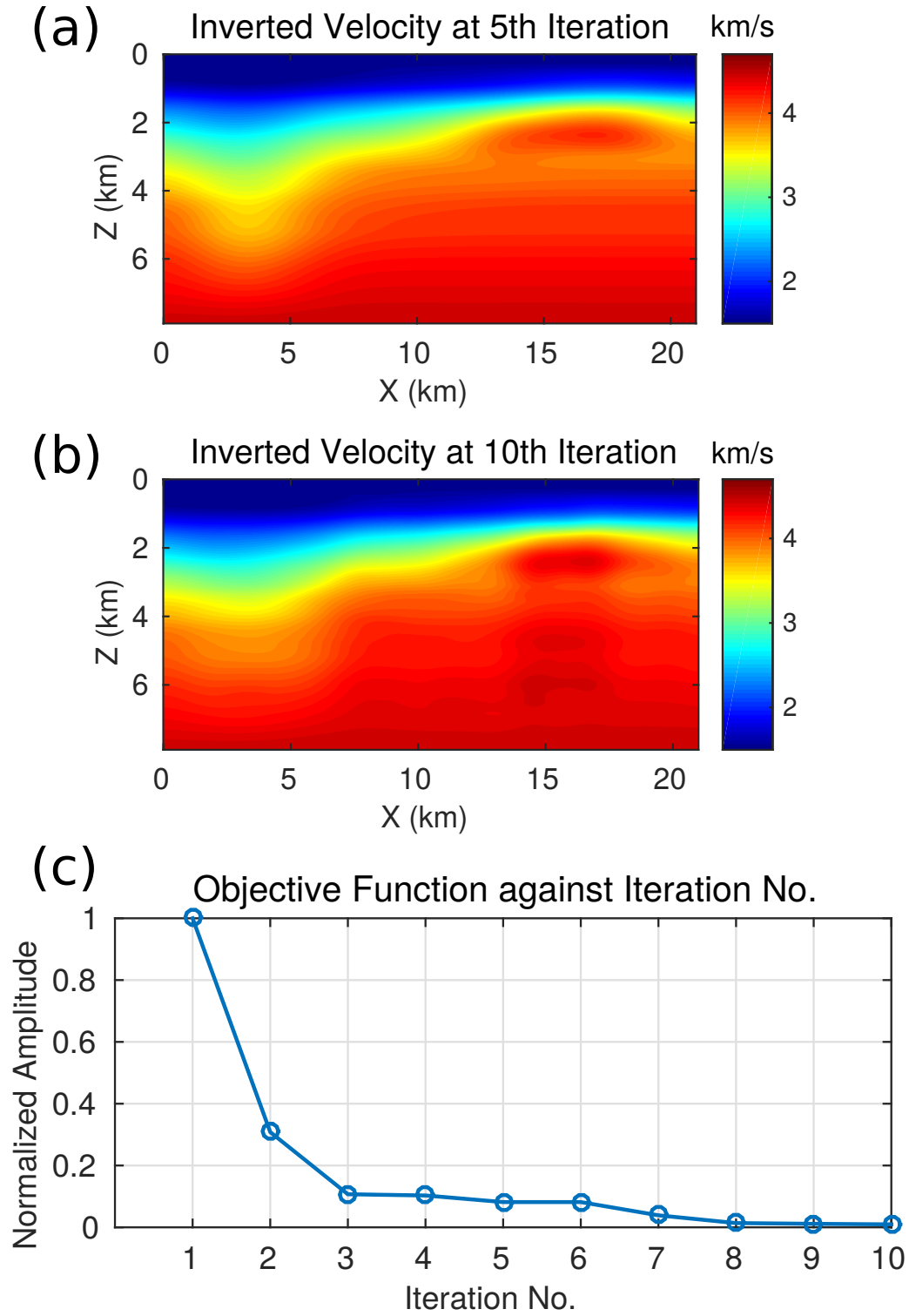


Figure 10: Inverted velocity model after (a) 5 iterations and (b) 10 iterations. Panel (c) shows the objective function at each iteration.

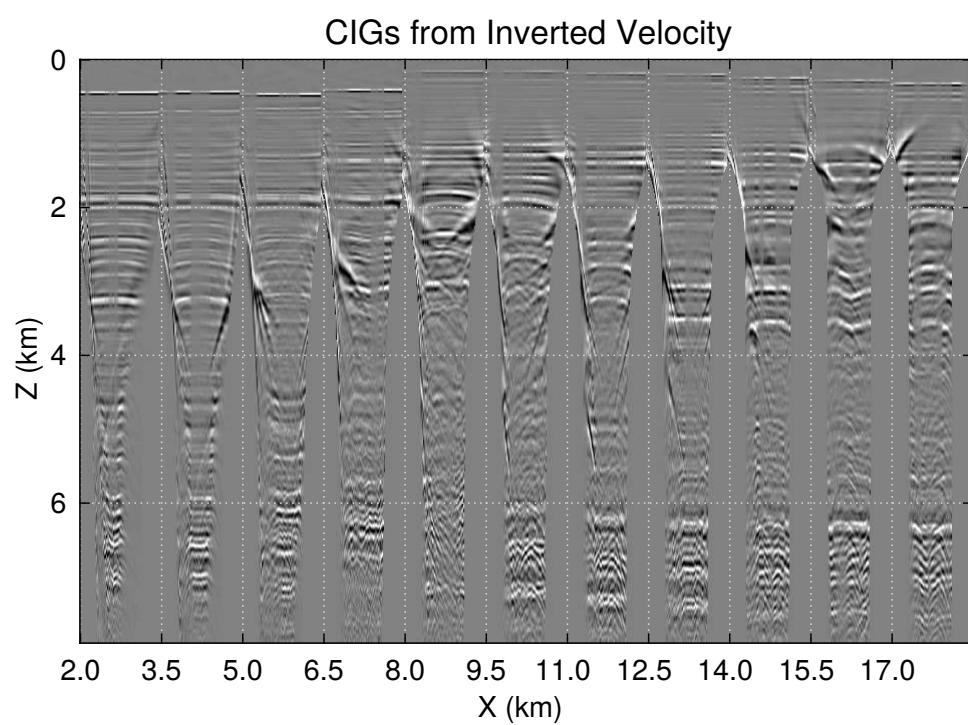


Figure 11: Plane-wave CIGs using the inverted velocity model shown in Figure 10b.
Guo & Schuster –

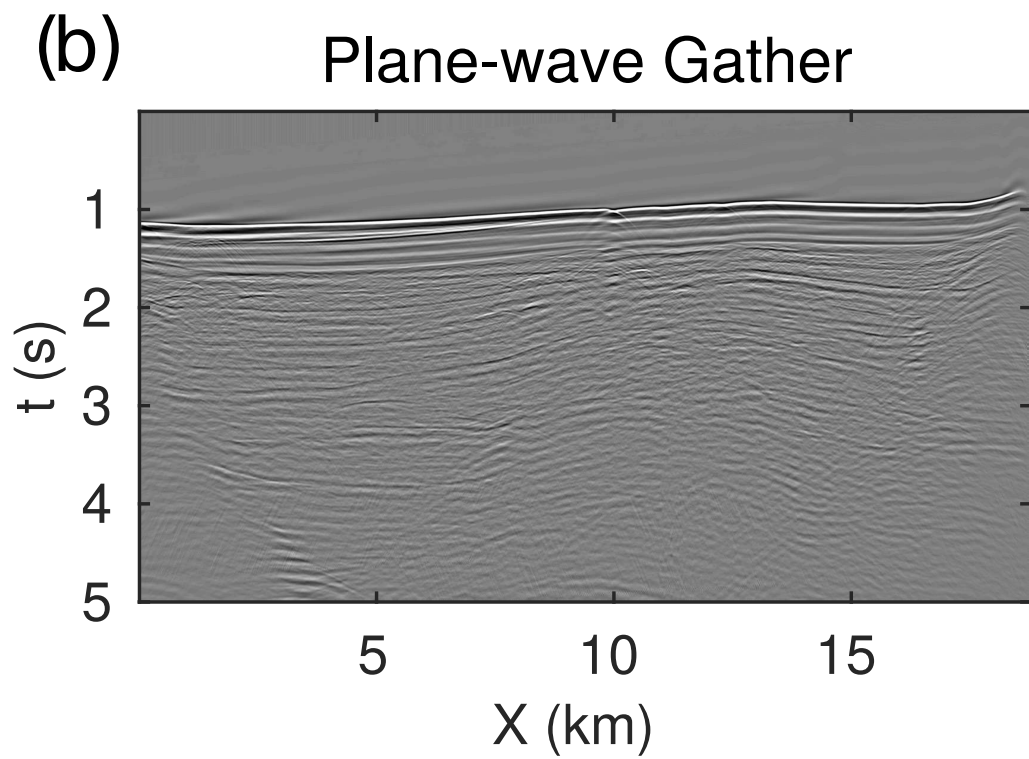
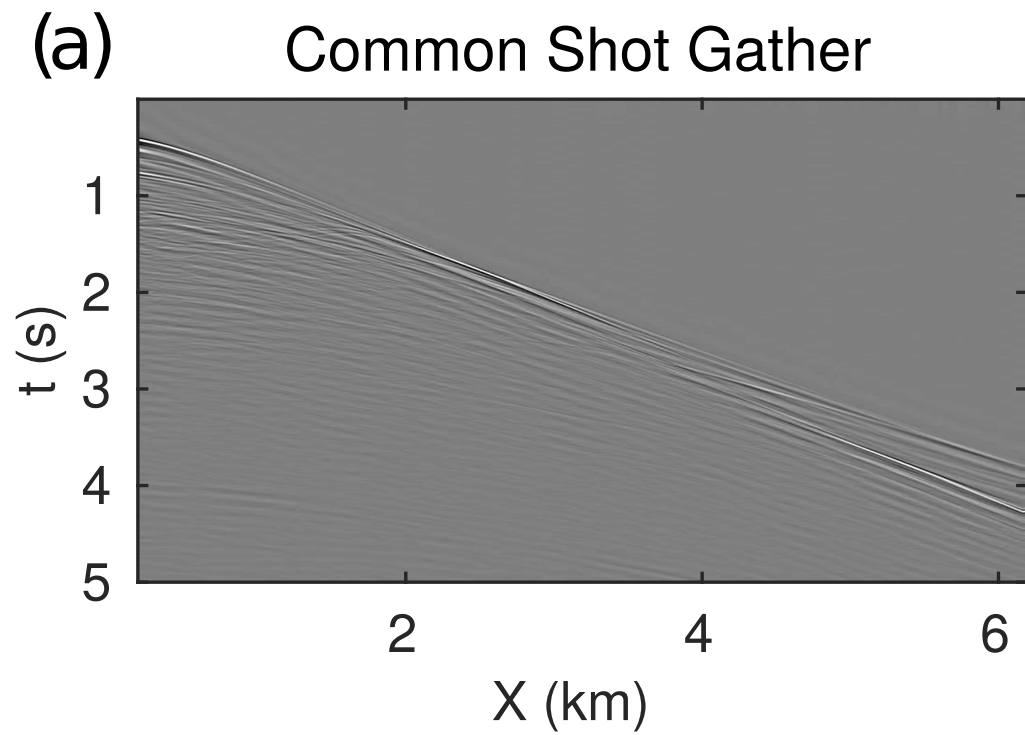


Figure 12: (a) A CSG recorded in the Gulf of Mexico data and (b) a plane-wave gather with $p = -0.04$ s/km.

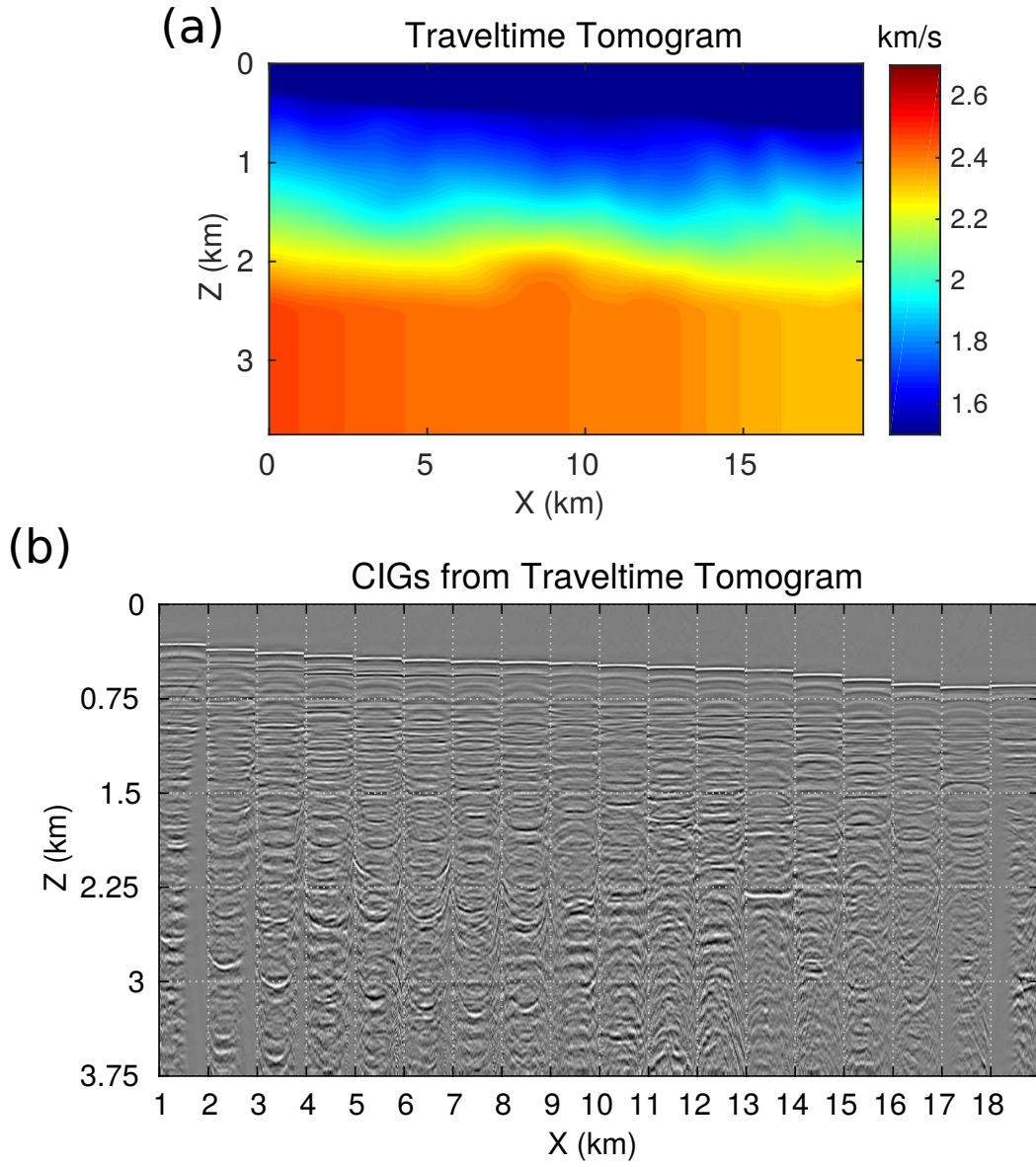


Figure 13: (a) The initial velocity model computed by inverting the traveltimes of the first arrivals and (b) the associated plane-wave CIGs.

Guo & Schuster –

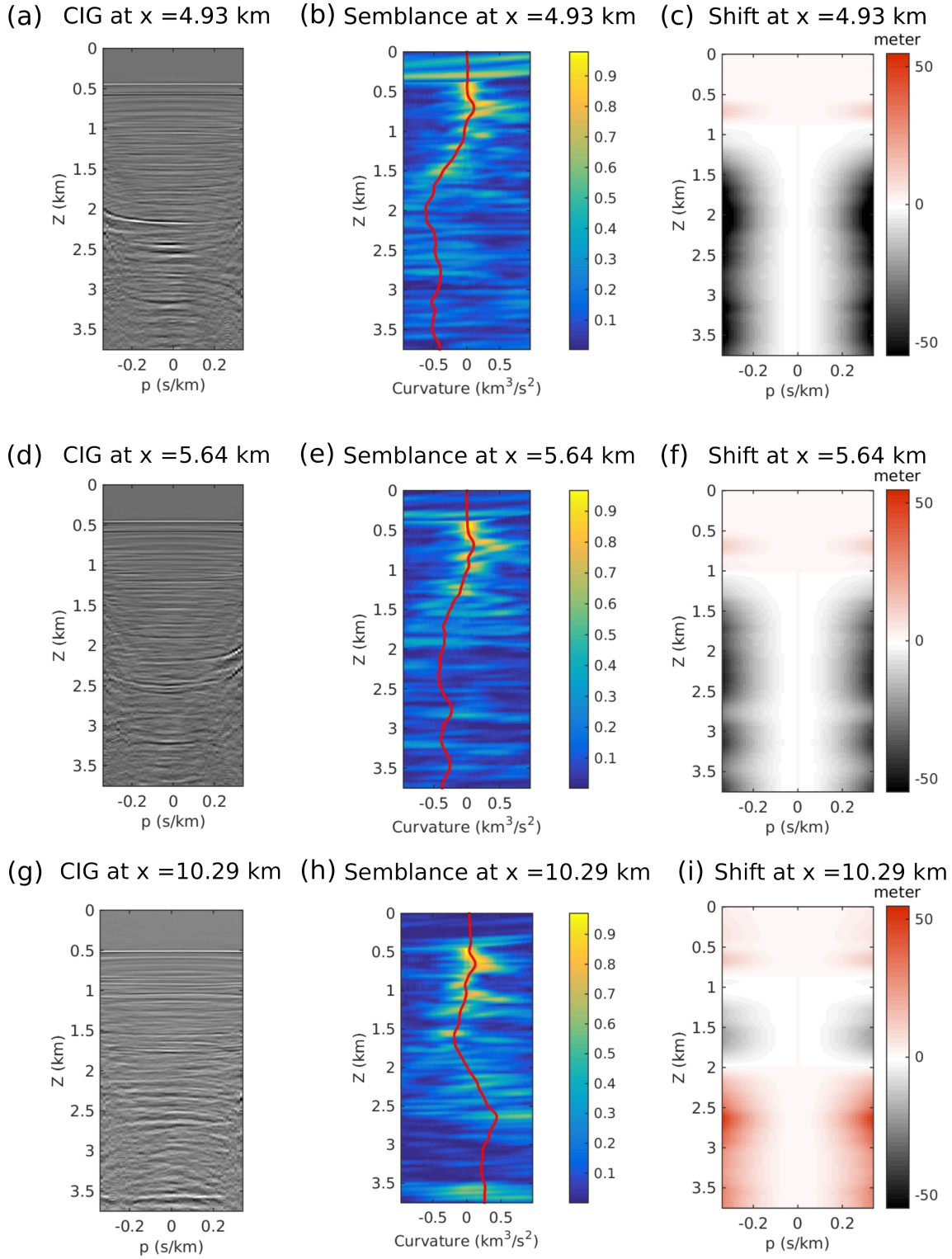


Figure 14: Plane-wave CIGs are used to calculate the semblance spectra and the shifts of CIGs.

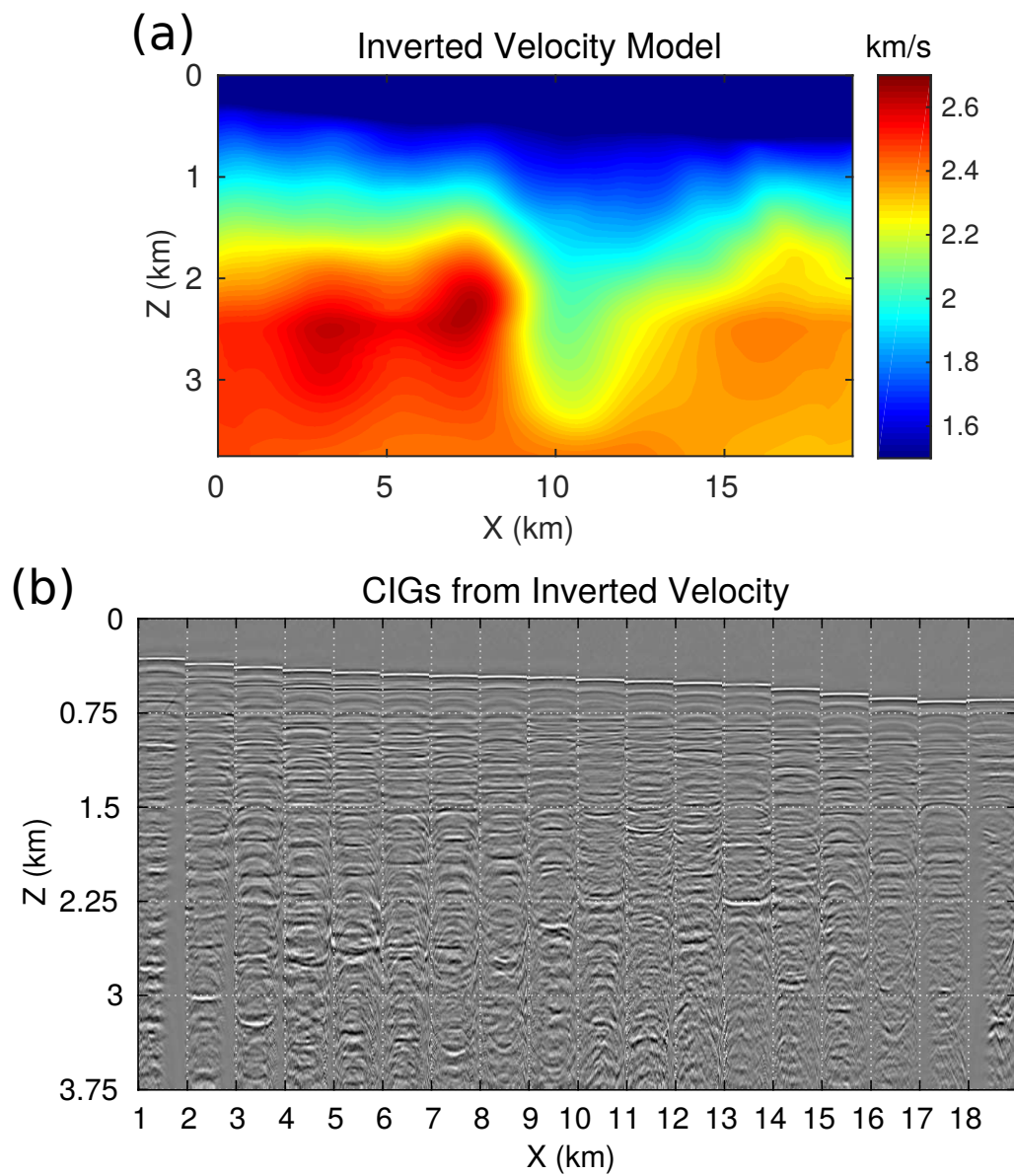


Figure 15: (a) The inverted velocity model after 10 iterations and (b) the associated plane-wave CIGs.

Guo & Schuster –

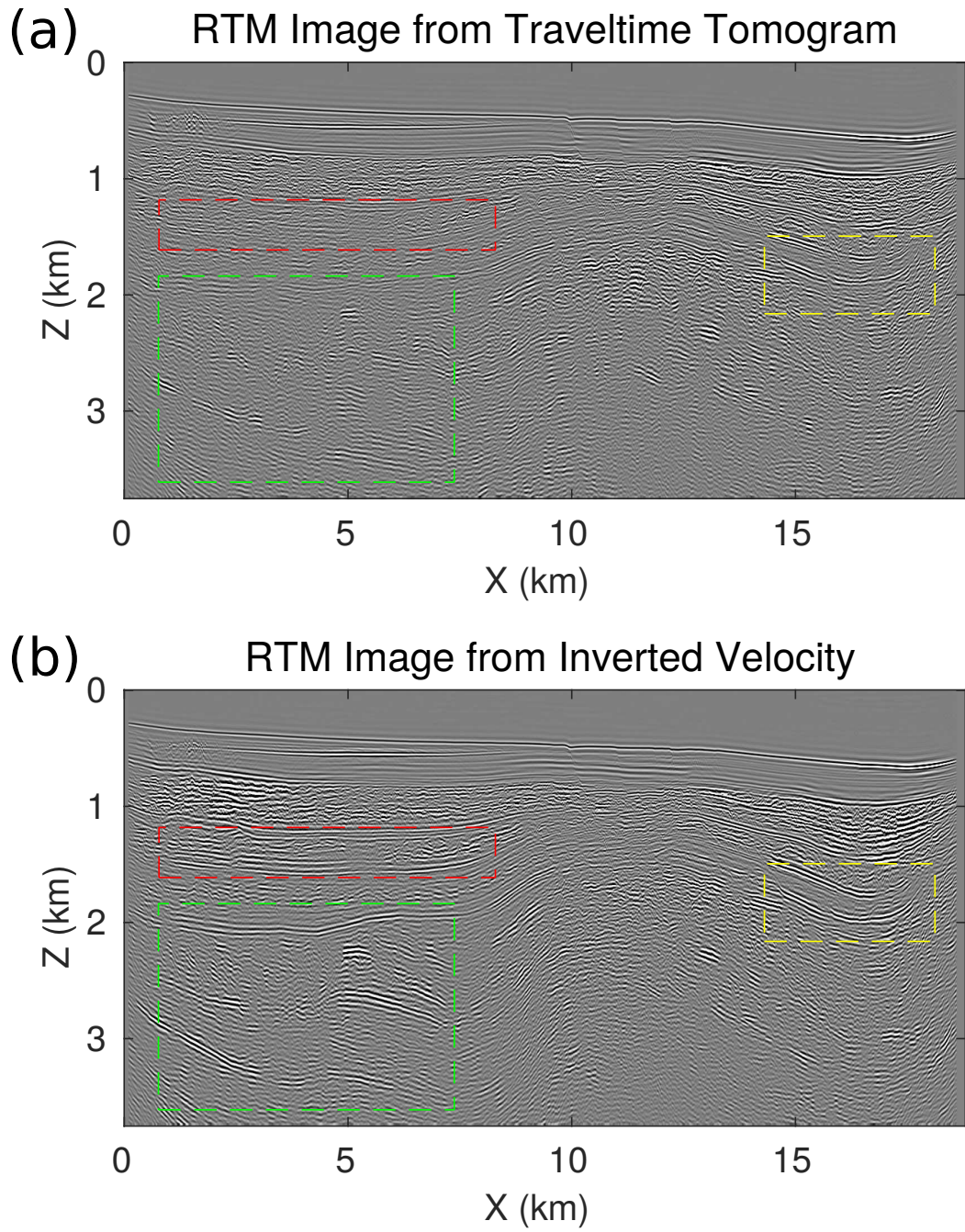


Figure 16: Shot profile RTM images based on the (a) traveltime tomogram in Figure 13a and (b) inverted velocity model shown in Figure 15a.

Guo & Schuster –

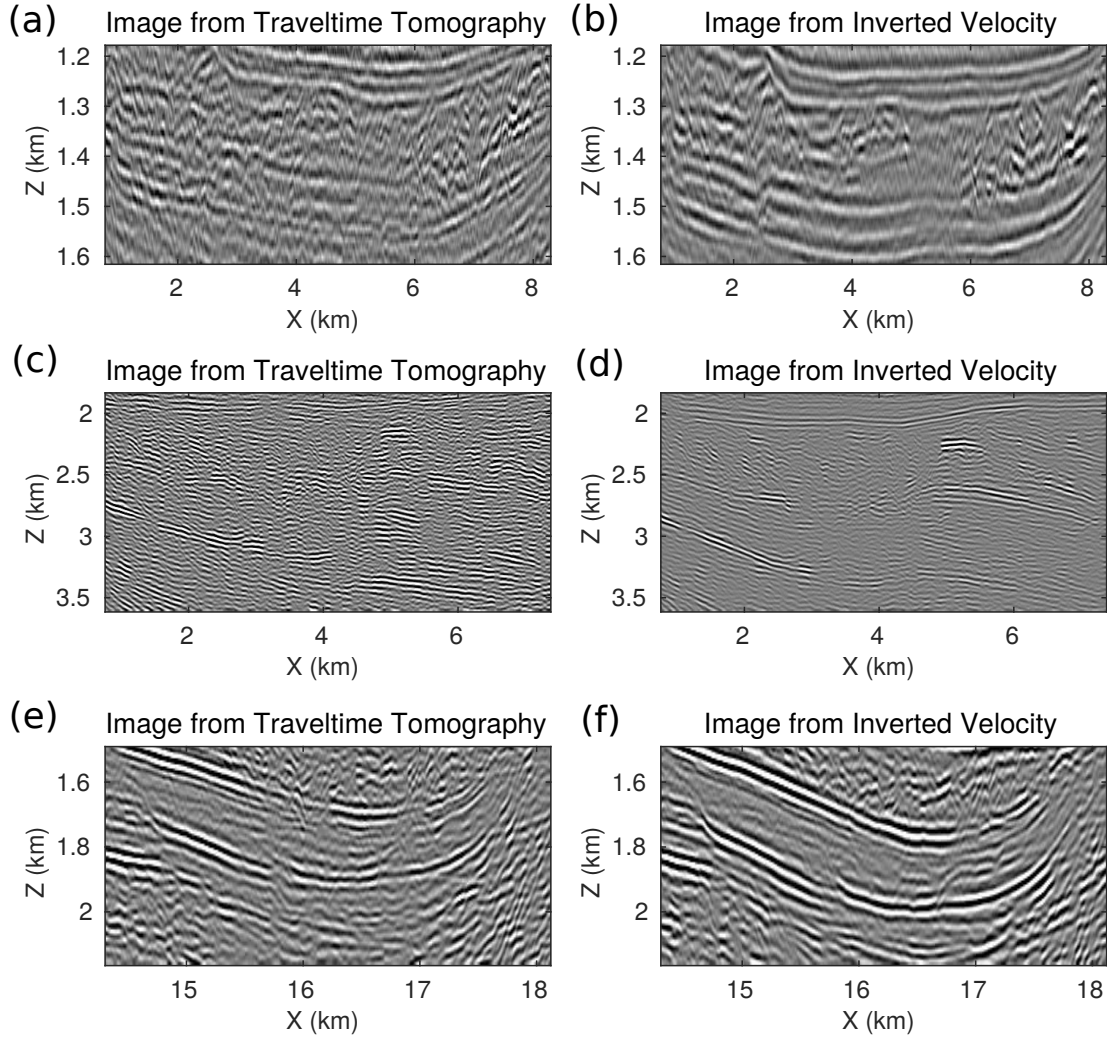


Figure 17: (a), (c), and (e) are the zoom-in view of the red, green and the yellow squares in Figure 16a, respectively. (b), (d), and (f) are the zoom-in view of the red, green and the yellow squares in Figure 16b, respectively.

Guo & Schuster –

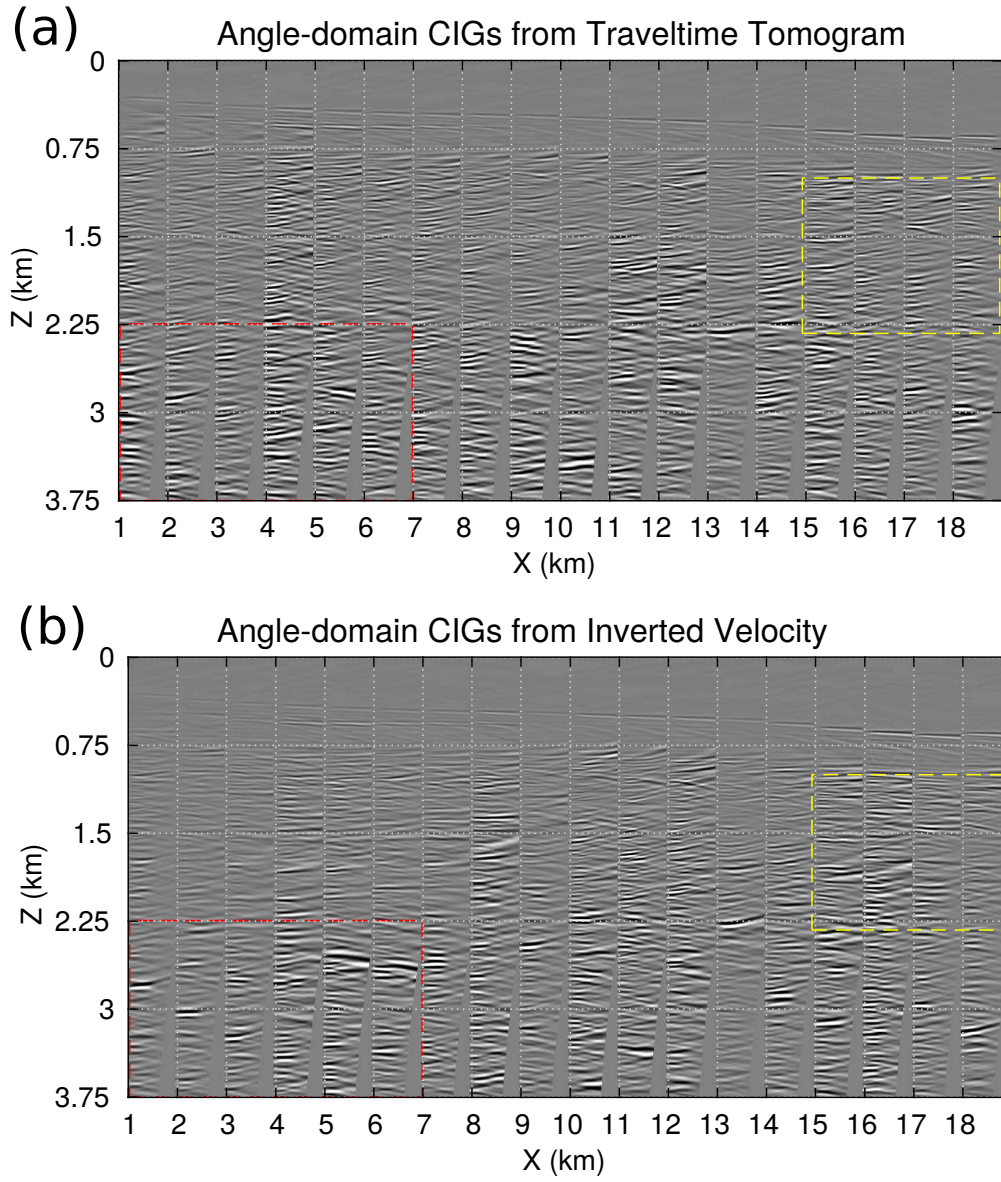
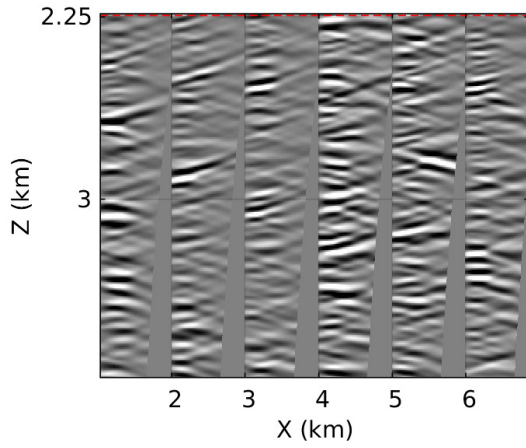


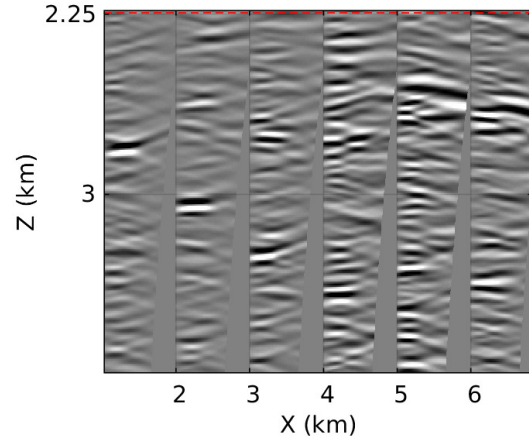
Figure 18: Angle-domain CIGs calculated from the (a) traveltime tomogram in Figure 13a and (b) inverted velocity shown in Figure 15a.

Guo & Schuster –

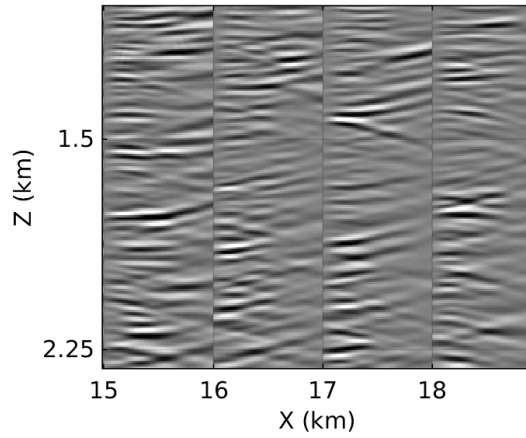
(a) Angle-domain CIG from
Traveltime Tomogram



(b) Angle-domain CIG from
Inverted Velocity



(c) Angle-domain CIG from
Traveltime Tomogram



(d) Angle-domain CIG from
Inverted Velocity

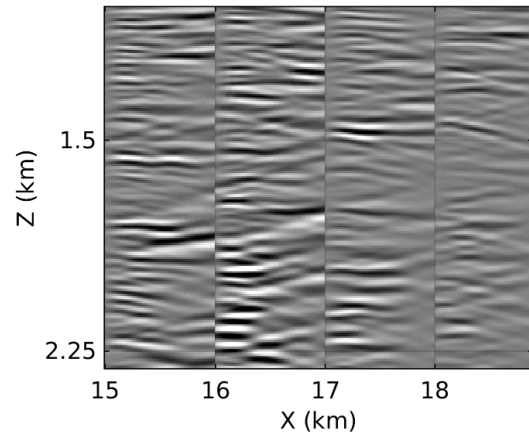


Figure 19: (a) and (c) are the zoom-in view of the red and the green squares in Figure 18a. (b) and (d) are the zoom-in view of the red and the green squares in Figure 18b.

Guo & Schuster –